Eur. Phys. J. A (2015) **51**: 22
DOI 10.1140/epja/i2015-15022-3

THE EUROPEAN PHYSICAL JOURNAL A

Review

The fundamental role of fission during r-process nucleosynthesis in neutron star mergers

S. Goriely[a]

Institut d'Astronomie et d'Astrophysique, CP-226, Université Libre de Bruxelles, 1050 Brussels, Belgium

Received: 6 October 2014 / Revised: 12 February 2015
Published online: 27 February 2015 – © Società Italiana di Fisica / Springer-Verlag 2015
Communicated by U.-G. Meißner

Abstract. The rapid neutron-capture process, or r-process, is known to be of fundamental importance for explaining the origin of approximately half of the $A > 60$ stable nuclei observed in nature. Despite important efforts, the astrophysical site of the r-process remains unidentified. Here we study r-process nucleosynthesis in a material that is dynamically ejected by tidal and pressure forces during the merging of binary neutron stars. r-process nucleosynthesis during the decompression is known to be largely insensitive to the detailed astrophysical conditions because of efficient fission recycling, producing a composition that closely follows the solar r-abundance distribution for nuclei with mass numbers $A > 140$. Due to the important role played by fission in such a scenario, the impact of fission is carefully analyzed. We consider different state-of-the-art global models for the determination of the fission paths, nuclear level densities at the fission saddle points and fission fragment distributions. Based on such models, the sensitivity of the calculated r-process abundance distribution is studied. The fission path is found to strongly affect the region of heavy nuclei responsible for the fission recycling, while the fission fragment distribution of nuclei along the $A \simeq 278$ isobars defines the abundance pattern of nuclei produced in the $110 \lesssim A \lesssim 170$ region. The late capture of prompt fission neutrons is also shown to affect the abundance distribution, and in particular the shape of the third r-process peak around $A \simeq 195$.

1 Introduction

The r-process, or the rapid neutron-capture process, of stellar nucleosynthesis is invoked to explain the production of the stable (and some long-lived radioactive) neutron-rich nuclides heavier than iron that are observed in stars of various metallicities, as well as in the solar system (for a review, see ref. [1]). In recent years, nuclear astrophysicists have developed more and more sophisticated r-process models, trying to explain the solar system composition in a satisfactory way by adding new astrophysical or nuclear physics ingredients. The r-process remains the most complex nucleosynthetic process to model from the astrophysics as well as nuclear-physics points of view. The site(s) of the r-process is (are) not identified yet, all the proposed scenarios facing serious problems. Complex —and often exotic— sites have been considered in the hope of identifying astrophysical conditions in which the production of neutrons is large enough to give rise to a successful r-process. Progress in the modelling of type-II supernovae and γ-ray bursts has raised a lot of excitement about the so-called neutrino-driven wind environment. However, until now a successful r-process cannot be obtained *ab initio* without tuning the relevant parameters (neutron excess, entropy, expansion timescale) in a way that is not supported by the most sophisticated existing models [2,3]. Although these scenarios remain promising, especially in view of their potential to significantly contribute to the galactic enrichment [4], they remain handicapped by large uncertainties associated mainly with the still incompletely understood mechanism that is responsible for the supernova explosion and the persistent difficulties to obtain suitable r-process conditions in self-consistent dynamical explosion and neutron-star cooling models [3,5,6]. In addition, predictions of the detailed composition of the ejected matter remain difficult due to the remarkable sensitivity of r-process nucleosynthesis to uncertainties of the ejecta properties [1].

Early in the development of the theory of nucleosynthesis, an alternative to the r-process in high-temperature supernova environments was proposed. It relies on the fact that at high densities (typically $\rho > 10^{10}$ g/cm^3) matter tends to be composed of nuclei lying on the neutron-rich side of the valley of nuclear stability as a result of free-electron captures [7]. The astrophysical plausibility of this scenario in accounting for the production of the r-nuclides has long been questioned. It remained largely unexplored until the study of the decompression of cold neutronized

[a] e-mail: sgoriely@astro.ulb.ac.be

matter resulting from tidal effects of a black hole (BH) or a neutron star (NS) on a NS companion in a binary system [8–10].

Recently, special attention has been paid to NS mergers following the confirmation by hydrodynamic simulations that a non-negligible amount of matter, typically about 10^{-3} to $10^{-2} M_{\odot}$, can be ejected [11–20]. In contrast to the supernova site, investigations with growing sophistication have confirmed NS merger ejecta as viable sites for strong r-processing [1,15–18,20–25]. In particular, recent nucleosynthesis calculations [18] show that the combined contribution of both the dynamical (prompt) ejecta expelled during the binary NS-NS or NS-BH merger, as well as the neutrino and viscously driven outflows generated during the post-merger remnant evolution of the relic BH-torus systems lead to the production of r-process elements from $A \gtrsim 90$ up to thorium and uranium with an abundance distribution that reproduces extremely well the solar distribution, as well as the elemental distribution observed in low-metallicity stars [27–29]. Note, however, that the relativistic NS-NS merger simulations of ref. [20] for a soft nuclear Equation of State (EOS) shows a significant impact of neutrino reactions on the electron fraction Y_e in the dynamical ejecta of cases with delayed collapse of the merger remnant. In this case, in addition to heavy r-process elements ($A > 140$), nuclei with lower mass numbers may also be created in the dynamical ejecta. It is still unclear whether the observed effects apply similarly strongly to all high-density EOSs and all binary systems that lead to a delayed collapse of the merger remnant.

The ejected mass of r-process material, combined with the predicted astrophysical event rate (around $10^{-5}\,\mathrm{y}^{-1}$ in the Milky Way [26]) can account for the majority of r-material in our galaxy [15,16]. Nearly all of the ejecta are converted to r-process nuclei, whose radioactive decay heating leads to potentially observable electromagnetic radiation in the optical and infrared bands [23,30] with 100–1000 times fainter peak brightnesses than those of typical supernovae and durations of only days [15,16, 24,31]. These "macronovae" or "kilonovae" are intensely searched for (with a recent, possible first success [32,33]); their unambiguous discovery would constitute the first detection of r-material *in situ*. Despite the successful nucleosynthetic properties of NS mergers, the first galactic evolution models [4] tend to disfavour compact object mergers as a potential r-process site because of their incapacity to explain the existence of very low-metallicity r-process–rich stars due to time delay between the binary system formation and its coalescence. In addition, the significant amount of r-process material ejected by a single NS merger event leads to a large scatter in r-process enrichment that did not seem to be confirmed by observations. However, recent studies [34–39] have reconsidered the galactic or cosmic chemical evolution of r-process elements in different evolutionary contexts, and although they do not converge towards one unique quantitative picture, most of them arrived at the conclusion that double compact star mergers may be the major production sites of r-process elements.

In this specific r-process scenario, the number of free neutrons per seed nuclei can reach a few hundred. With such a neutron richness, heavy fissioning nuclei can be produced. For this reason, in this astrophysical site, fission plays a fundamental role, more particularly by i) recycling the matter during the neutron irradiation (or if not, by allowing the possible production of super-heavy long-lived nuclei, if any), ii) shaping the r-abundance distribution in the $110 \leq A \leq 170$ mass region at the end of the neutron irradiation, iii) defining the residual production of some specific heavy stable nuclei, more specifically Pb and Bi, but also the long-lived cosmochronometers Th and U, and iv) heating the environment through the energy released. Fission probabilities remains, however, extremely difficult to predict and consequently the impact of the fission processes on the r-process nucleosynthesis difficult to ascertain. In this paper, we present in sect. 2 recent r-process calculation in NS mergers and in sect. 3 some recent determination of the fission probabilities as well as fission fragment distribution (FFD). In sect. 4, we study the sensitivity of the various fission ingredients on the r-abundance distribution resulting from the prompt ejection of the NS merger material. In sect. 5, the uncertainties affecting the other two main nuclear inputs to nucleosynthesis predictions, *i.e.* the neutron capture and β-decay rates, are briefly discussed. The impact of fission on the nucleosynthesis of the Th and U cosmochronometers are discussed in sect. 6. Conclusions are drawn in sect. 7

2 NS merger simulations and the r-process

The NS-NS merger simulations considered in the present paper were performed with a general relativistic Smoothed Particle Hydrodynamics scheme [14,16,40] representing the fluid by a set of particles with constant rest mass, the hydrodynamical properties of which were evolved according to Lagrangian hydrodynamics, keeping the electon fraction (Y_e) of fluid elements fixed. The Einstein field equations were solved assuming a conformally flat spatial metric. It was shown in refs. [16,18] that if the amount of mass ejected, the ejecta velocity and the luminosity of the optical transient depend sensitively on the adopted NS mass ratios or EOS, invariably, more than 95% of the ejected material is predicted to be r-process rich with a distribution that is virtually identical for all the systems (at least assuming neutrino effects do not significantly affect the electron fraction distribution [20]). For this reason, in the present analysis, only the symmetric $1.35 M_{\odot}$–$1.35 M_{\odot}$ system with the DD2 EOS [41] and a resolution of about 550000 particles is considered. Note that the $1.35 M_{\odot}$–$1.35 M_{\odot}$ case is of particular interest since, according to population synthesis studies and pulsar observations, it represents the most abundant systems [42]. The corresponding NSs have radii of $\sim 13.2\,\mathrm{km}$ and the mass ejected from the system is about $3\ 10^{-3} M_{\odot}$ (see ref. [16] for more details on the gross properties of the ejecta and the influence of the EOS). Note that the maximum NS mass resulting from this EOS amounts to $2.4 M_{\odot}$ in agreement with recent observations of a $2 M_{\odot}$ NS [43,44].

The ejected "particles" (*i.e.* mass elements) originate mostly from two different regions in the inner crust of the initial stars. About $\sim 75\%$ of the material are squeezed out from the contact interface of the NSs. The remaining 25% are ejected from the near-surface regions close to the orbital plane. All ejecta have low Y_e ranging between 0.015 and 0.050. For the first 27 ms the density history is consistently followed by the numerical simulation. Afterwards the escaping ejecta are assumed to expand freely with constant velocity. The radii of the ejecta clumps thus grow linearly with time t and their densities drop like $1/t^3$ (for more details, see refs. [15,16]).

The ejected matter is initially cold, but most of it gets shock-heated just prior to the ejection to temperatures above 1 MeV. As soon as the expansion takes place, the temperature drops. Later shocks can reheat the matter and increase the density. After the drip density is reached ($\rho_{\rm drip} \simeq 4.2 \times 10^{11}$ g/cm^3), a complex temperature profile is still present due to the interaction between the various mass elements. Mass elements with very different density and temperature profiles are found in the relativistic simulations, leading to potential variations in the concomitant nucleosynthesis. When the density has dropped below the drip density and the temperature has dropped below 10^{10} K, the nucleosynthesis starts to be followed with a full reaction network (see below). The initial composition is then determined from the nuclear statistical equilibrium at the given density, temperature and electron fraction. The temperature evolution is further determined on the basis of the laws of thermodynamics, allowing for possible nuclear heating through β-decays, fission, and α-decays, as described in ref. [10].

For each simulation, about 200 representative trajectories are processed, which roughly correspond to about one sixth of the total ejecta. Comparing the final abundance distributions for about 200 and the full set of 1200 fluid-element histories reveals a very good quantitative agreement, which proves that a properly chosen sample of about 200 trajectories is sufficient to be representative for the total amount of unbound matter.

The r-process nucleosynthesis is calculated with a reaction network including all 5000 species from protons up to $Z = 110$ lying between the valley of β-stability and the neutron drip line. All charged-particle fusion reactions on light and medium-mass elements that play a role when the nuclear statistical equilibrium freezes out are included in addition to radiative neutron captures and photodisintegrations. The reaction rates on light species are taken from the NETGEN library, which includes all the latest compilations of experimentally determined reaction rates [45]. Experimentally unknown reactions are estimated with the TALYS code [46–48] on the basis of the Skyrme Hartree-Fock-Bogolyubov (HFB) nuclear mass model, HFB-21 [49]. On top of these reactions, β-decays as well as β-delayed neutron emission probabilities are also included, the corresponding rates being taken from the updated version of the Gross Theory [50] based on the same HFB-21 Q-values. As shown below, fission processes, including neutron-induced, spontaneous, β-delayed and photofission are carefully introduced in the network together with the corresponding FFD. Note that all fission products with a yield larger than typically 10^{-5} are linked to the parent fissioning nucleus in the network calculation, *i.e.* about 500 fission fragments are included for each fissioning nucleus. The n-rich fission fragments located outside the network, *i.e.* across the neutron drip line, are assumed to instantaneously emit neutrons down to the neutron drip line. The total mass fraction as well as number of nucleons is conserved at all time and the emitted neutrons are recaptured consistently by all the existing species. Finally, α-decays are taken into account for all heavy species, the rates being extracted from ref. [51].

3 Fission calculation

Since its discovery, fission has always been an active field of research both regarding its purely theoretical challenge and its practical applications. Almost all existing evaluations of the neutron-induced fission cross sections rely on the multiple-humped fission penetration model where barriers are described by inverted decoupled parabolas. Such approaches consider all ingredients as free parameters in order to be able to achieve more or less accurate fits to experimental cross sections [52,53]. Although such adjustments respond to the needs of some nuclear applications, their predictive power remains poor due to the large number of free parameters; these methods cannot be used in applications requiring a purely theoretical description of fission for experimentally unknown nuclei, such as nuclear astrophysics. For this reason, the prediction of fission cross section is far from being satisfactory nowadays. Recent studies aim at providing sounder descriptions of some of the basic nuclear ingredients required to describe fission cross sections. These concern in particular fission barriers (or more generally fission paths) and nuclear level densities (NLD) at the fission saddle points, but also fission fragment distribution, including the average number of emitted neutrons. Recently, such nuclear ingredients have been systematically determined in the framework of nuclear astrophysics applications, as described below.

3.1 Fission path

Detailed fission paths have been recently determined on the basis of the Skyrme-HFB model [54] which has proven its capacity to estimate the static fission barrier heights with a relatively high degree of accuracy. The HFB model corresponds to a standard mean-field calculation based on an effective Skyrme interaction. Of particular interest for fission application, the calculation includes all axially symmetric quadrupole, octupole and hexadecapole deformation degrees of freedom, as well as a semi-microscopic quadrupole correlation energy based on the cranking model. Note that such a cranking approximation of the rotational correlation energy has been shown [55] to agree with the exact calculation of Bender *et al.* [56] and reproduce fairly well experimental moments of inertia. It also includes a high-deformation part for the vibrational correction that is not absorbed into the Skyrme

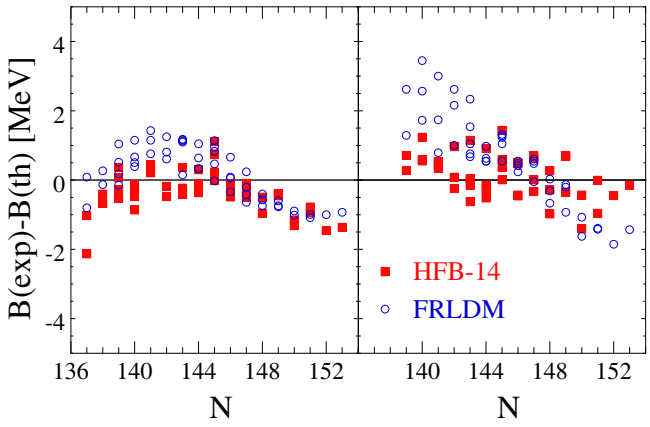

Fig. 1. (Color online) Deviations between the empirical fission barriers [61] and those predicted by the HFB-14 (squares) and FRLDM (circles) model for the primary (left panel) and secondary (right panel) barriers for nuclei with $88 \leq Z \leq 96$.

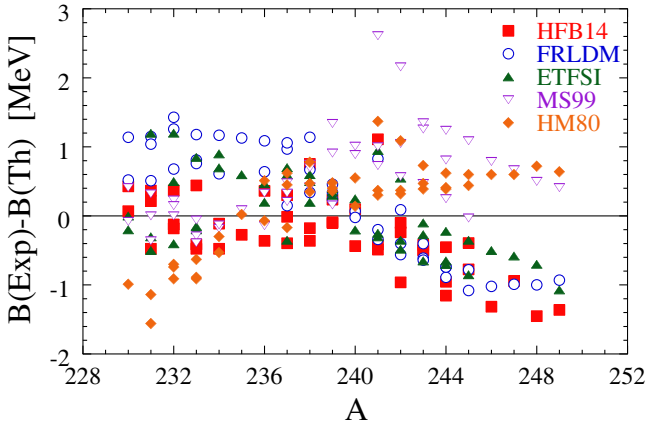

Fig. 2. (Color online) Deviations between 45 empirical primary fission barriers [61] and those predicted by the HFB-14 [54], FRLDM [62], ETFSI [63], MS99 [64] and HM80 [65] global models for $88 \leq Z \leq 96$.

part of interaction, as detailed in ref. [54]. This quadrupole correlation energy has also been shown to be in rather good agreement with the 5-dimensional collective Hamiltonian results obtained with the Gogny D1M interaction for all even-even nuclei [49]. The strong deformation dependence of this quadrupole correlation energy turns out to be crucial for a proper description of the nuclear surface at large deformations [54]. Also note that for odd number of nucleons, the equal filling approximation [57] is adopted for the fission path calculation, as done in the HFB mass model. It should be emphasized that the HFB calculation of fission path is based on the BSk14 Skyrme interaction and represents an extension calculation in the deformation plane of the HFB-14 mass model that reproduces all experimental atomic masses with a high accuracy, namely with an rms deviation of 0.739 MeV with respect to the 2353 known masses in the 2012 atomic mass evaluation [58]. Clearly, more sophisticated calculation of fission barriers, including finite-range interactions or correlation energies based on the generalized coordinate method exist (see in particular refs. [59,60]), but the HFB-14 model has the merit to provide fission paths for all the 2000 nuclei of interest for the r-process simulations and has shown its capacity to reproduce fairly accurately all ground state energies and other nuclear structure properties. The fission barriers determined within the HFB-14 model [54] reproduce the 52 primary empirical barriers (*i.e.* the highest barriers of prime interest in cross section calculations) of nuclei with $88 \leq Z \leq 96$ with an rms deviation as low as 0.67 MeV. A similar accuracy is obtained (0.65 MeV) for the secondary barriers. The HFB-14 barriers are compared with the empirical ones [61] in fig. 1 where differences up to 1 MeV on the highest barrier can be observed. The HFB-14 model generally overestimates the height of the primary barrier, so that a global decrease of the energy surface may be required (see sect. 3.3). Similar deviations are obtained within the macroscopic-microscopic approach with the Finite-Range Liquid Drop Model (FRLDM) [62], in particular for primary barriers (an rms deviation of 0.77 MeV being obtained with respect to empirical barriers). In contrast, for secondary barriers, rather larger deviations are found by FRLDM with an rms deviation of 1.41 MeV. Such a large difference may obviously have a significant impact on fission probabilities. However, at this stage, no theoretical models can claim to provide predictions of barrier heights with a global accuracy better than 0.5–1 MeV (in the best case). As shown in fig. 2, similar types of deviations are found with the other global models available. These concern the Extended-Thomas-Fermi plus Strutinsky Integral (ETFSI) model [63], the Thomas-Fermi model [64] (hereafter MS99) as well as the droplet model of Howard and Möller [65] (hereafter HM80). With respect to the 45 empirical primary fission barriers[1] shown in fig. 2, the rms deviation amounts to 0.6 MeV for HFB-14, 0.81 MeV for FRLDM, 0.57 MeV for ETFSI, 0.82 MeV for MS99 and 0.66 MeV for HM80. This comparison clearly shows that there is still a lot of room for improvement of global models in the prediction of fission barriers. Additional work within the Skyrme HFB framework has recently been performed, but without including corrections beyond mean field [66]. Such corrections are strongly deformation dependent, so that they influence not only the predictions at the fission saddle points but also in the isomeric well.

In comparison with other available compilation of fission barriers, HFB-14 barrier predictions are relatively high, as shown in fig. 3. Already for nuclei close to the stability, the HFB-14 are higher than those predicted by the FRLDM model [62] which drops below 5 MeV for $N > 155$. For exotic neutron-rich nuclei across the $N = 184$ shell closure, HFB-14 fission barriers are compared in fig. 3 with the ETFSI and MS99 predictions. HFB-14 barriers show a pronounced shell effect around $N = 184$, though less than does the ETFSI barriers which are usually higher, except in the $N \simeq 170$ region. In

[1] This subset for 45 nuclei out of 52 accounts for barriers that have been provided by all the above-mentioned models.

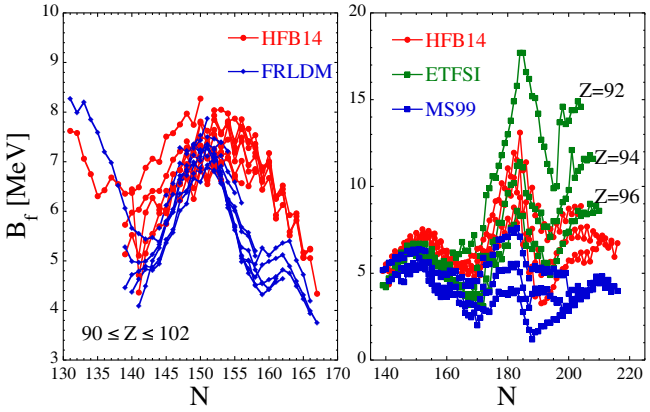

Fig. 3. (Color online) Left: Comparison between the HFB-14 and FRLDM primary barriers [62] for even-Z isotopic chains relatively close to the valley of stability. Right: Same for the HFB-14, ETFSI [63] and MS99 model [64] barriers for $Z = 92$, 94 and 96 isotopes up to the neutron drip line.

contrast, the MS99 barriers are by far the lowest with heights between 3 and 5 MeV for the most exotic nuclei. These differences can have a significant impact on fission rate (sect 3.3) as well as nucleosynthesis (sect. 4) predictions. Note that for neutron-rich nuclei with $Z \gtrsim 100$ and lying close to the neutron drip line, only HFB-14 barriers are available.

The HFB-14 fission path projected on the quadrupole deformation are illustrated in the upper panel of fig. 4 for the Cm isotopes close to the valley of β stability. The fission path corresponds to the most gently climbing or steepest descending path found and projected along one deformation parameter, namely the quadrupole deformation β_2 (see ref. [54] for more details). Note that more sophisticated ways to estimate the fission path exist, in particular on the basis of the least-action principle (see, *e.g.*, refs. [59,60,67]), which are known not to affect drastically fission barrier heights, but have a drastic impact on fission half-lives. The fission path for these nuclei appears to be well represented by a traditional double-humped barrier, at least locally close to the saddle point deformations. The situation can be quite different as soon as we depart from the valley of stability. As shown in the middle and lower panels of fig. 4, the fission path for exotic neutron-rich nuclei cannot, in general, be simply approximated by a double-humped barrier with parabolic shapes. To estimate the transmission coefficients with fission barriers deviating from the simple inverted parabolic picture, the full WKB method needs to be applied [68].

The fission paths have been estimated within the HFB model with BSk14 Skyrme force for all nuclei with $90 \leq Z \leq 110$ lying between the valley of β-stability and the neutron drip lines, *i.e.* about 2000 nuclei. The primary barriers are shown in fig. 5. All the fission paths are available in a table and graphical format in the BRUSLIB nuclear library [45]. In the present study, only the HFB-14 and MS99 sets of fission barriers are considered, since they represent the only data publicly available covering all the $Z \leq 110$ nuclei from the valley of β-stability to the neutron

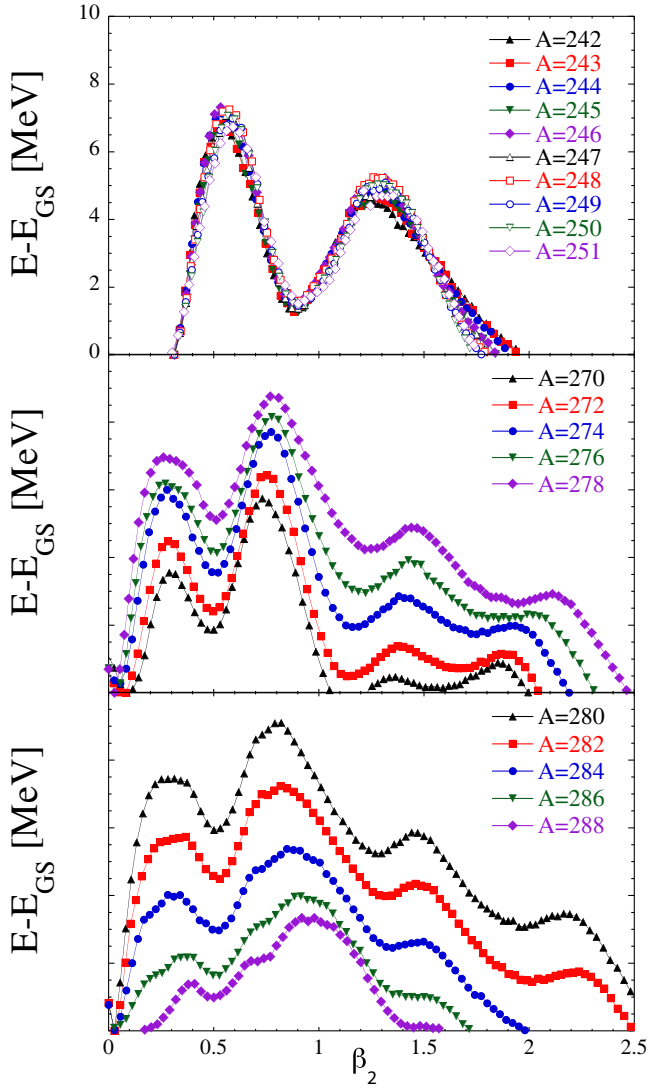

Fig. 4. (Color online) Fission path (*i.e.* total energy with respect to the ground-state energy E_{GS}) as a function of the quadrupole deformation parameter β_2 for the Cm isotopes lying close to the valley of β stability (upper panel) or in the neutron-rich region (middle and lower panels).

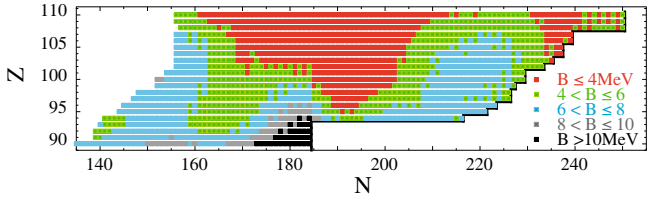

Fig. 5. (Color online) Representation in the (N, Z) plane of the height of the primary fission barrier (in MeV) predicted by the HFB-14 model. The solid line represents the HFB-21 neutron drip line [49].

drip line. The HM80 macroscopic-microscopic model has also been applied to the large-scale calculation of fission barriers for neutron-rich nuclei up to $N = 184$ [65] but is restricted to $Z \leq 100$ elements and cannot be applied to nucleosynthesis for this reason. Similarly, the FRLDM compilation [62] does not include nuclei up to the neutron drip line.

3.2 NLD at the saddle points

The above-mentioned HFB calculations also provide all the necessary ingredients to estimate the NLD. On the basis of the single-particle scheme and pairing strength of the same HFB-14 model that was used to determine the HFB-14 mass table and the fission path, a very satisfactory prediction of the NLD in the ground-state configuration was obtained within the combinatorial method at the neutron binding energy for both the s- and p-wave data [69]. The very same model has been used to estimate coherently the spin- and parity-dependent NLD at the fission barriers on the basis of the HFB-14 single-particle level scheme and pairing strength at the corresponding deformations of both the inner and outer saddle points (more details can be found in refs. [45,61]). It should, however, be mentioned that if the NLD is rather well constrained by the HFB structure properties (though still affected by the complicated task to determine the saddle point deformation), the inclusion of the phonon excitations is still subject to a rather large uncertainty. Due to the lack of observables, the same prescription is used for the saddle points as for the ground state, *i.e.* a total of 3 phonons have been coupled to the excitation configurations of maximum 4 particle-holes. Quadrupole, octupole and hexadecapole phonons are included, their energies being assumed identical to those of the ground state. This prescription leads to a damping of the NLD vibrational enhancement factor at a relatively low energy (typically 10 MeV). This damping prescription, especially on the ground-state NLD of the target nucleus, can have a rather large impact on the first-chance fission cross section at energies above typically 10 MeV [61,69]. Finally, note that the second and third saddles as well as the second minimum are found to be left-right asymmetric within the HFB framework. For these reasons, the NLD are multiplied by a factor 2 [61]. In contrast, the inner barrier and first isomer may be triaxial, as suggested by mean-field calculations [59,66], though in the HFB-14 approach, it has been estimated within the approximation of an axial symmetry. For those cases, the corresponding enhancement factor as given in ref. [61] (see their eq. (209)) needs to be considered.

The combinatorial model has been shown [69] to give rise to some complex structures linked to the shell, pairing, and deformation effects, in contrast to the smooth behaviour of phenomenological expressions traditionally used [70]. Such complex structure remains to be confirmed since they may well represent some artifacts linked to missing correlations [71]. There is, however, no direct experimental data that can be used to test NLD at the saddle points. The combinatorial NLD at the ground state and fission saddle points have been tested in the calculation of neutron-induced fission cross section [68] and shown to lead to satisfactory agreement with experimental data. The NLD at the fission saddle points for all nuclei with $90 \leq Z \leq 110$ from the valley of β-stability to the neutron drip line can be found in a table and graphical format in the BRUSLIB library [45].

3.3 Fission rates

The neutron-induced fission cross sections and astrophysical rates have been estimated on the basis of the TALYS code [46–48]. TALYS is a software for the simulation of nuclear reactions, which includes many state-of-the-art nuclear models to cover all main reaction mechanisms encountered in light particle-induced nuclear reactions. TALYS provides a complete description of all reaction channels and observables and in particular takes into account all types of direct, pre-equilibrium, and compound mechanisms to estimate the total reaction probability as well as the competition between the various open channels. The code is optimized for incident projectile energies, ranging from 1 keV up to 200 MeV on target nuclei with mass numbers above 12. It includes photon, neutron, proton, deuteron, triton, ^{3}He, and α-particles as both projectiles and ejectiles, and single-particle as well as multiparticle emissions and fission.

Many of the TALYS default input parameters are taken from the RIPL database [61] (*e.g.* nuclear masses, low-energy discrete levels, gamma widths, resonance spacings), but for experimentally unknown nuclei, microscopic or semi-microscopic nuclear models have been adopted [45]. The above-mentioned fission ingredients have been tested in neutron-induced fission cross section calculations [68,73]. An uncertainty of the order of 1 MeV on the fission barrier height is known to have a significant impact on the fission cross section. For data evaluation purposes, it is possible to adjust the nuclear ingredients to reproduce at best the cross sections. In particular, the inner and outer barrier heights can be scaled coherently, without modifying the fission path topology, and the NLD at each saddle points renormalized in a way similar as done with the ground-state NLD [69].

The fission transmission coefficients are estimated within the so-called WKB approximation, as detailed in ref. [68]. Of relevance in such calculation is also the calculation of the collective inertial mass which is not estimated from the HFB calculation at the present time, but approximated by the semi-empirical expression $\mu = 0.054\ A^{5/3}\,\mathrm{MeV}^{-1}$ and assumed to be independent of the deformation parameter. Future global calculations should consistently consider the HFB estimates of the inertial mass. We compare in fig. 6 the experimental neutron-induced fission cross sections for the different U isotopes with the calculation based on the renormalized microscopic input. It should be stressed that these calculations have been performed in the 1 keV to 30 MeV range making a coherent use of one unique set of renormalization parameters independently of the channel or target considered.

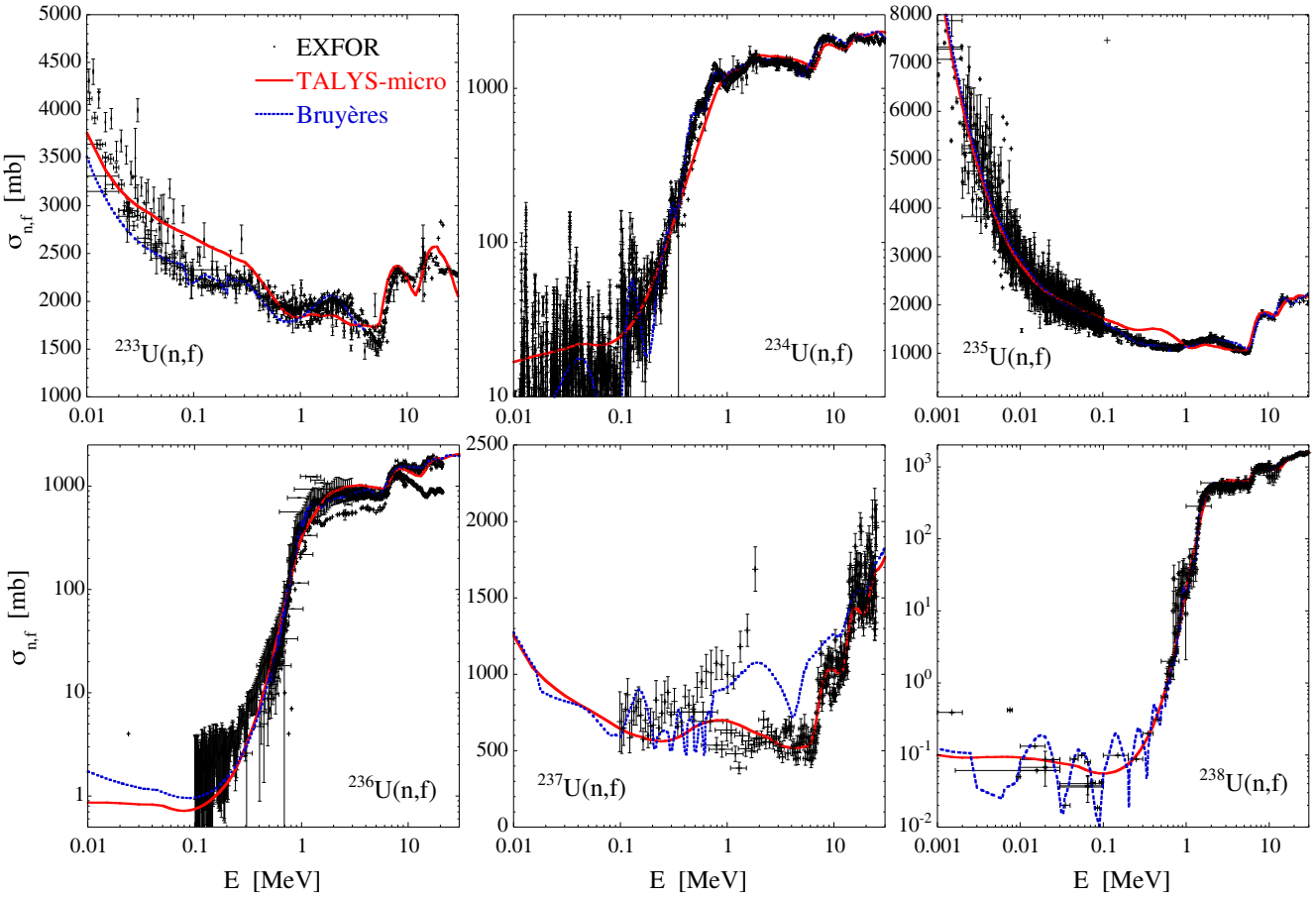

Fig. 6. Neutron-induced fission cross sections (solid line) obtained with renormalized HFB fission paths and HFB plus combinatorial NLD. The dotted line corresponds to the fit of the Bruyères-le-Châtel group [53]. Experimental data are taken from the EXFOR library [72].

The use of one unique set of input parameters to describe all channels for all U isotopes also enhances the credibility of the physics behind such a calculation. In fig. 6, the cross sections are also compared with the optimal fit obtained by the Bruyères-le-Châtel group [53]. These fits correspond to some of the best ones that can be achieved nowadays on the basis of highly parametrized phenomenological models. Note, however, that the number of free parameters in such evaluations is about five times larger than the number of renormalization parameters used in the microscopic approach (more details can be found in ref. [73]). Including additional parameters, such as discrete transition and class-II/III states, and further improving the description of the transmission and absorption through the barrier, should lead to cross section fits that are of the same level accuracy as the best phenomenological calculations available today. Microscopic models are, however, in essence very different than the phenomenological models traditionally used, so although similar fits to known data are achieved, non-negligible differences may be expected for nuclei, energy ranges, or reaction channels for which no data exist. Such a test on the fission ingredients shows that the various inputs can be tuned to reproduce at best experimental data in one unique coherent framework, which was far from being obvious a priori. It represents a necessary condition for judging the quality of the fission ingredients.

Now turning to the *prediction* of fission cross section, if use is made of the default HFB fission paths and NLD, cross section can be estimated within more or less of factor of 10 with respect to experimental data [68]. The largest uncertainty obviously comes from the 0.5–1 MeV uncertainty on the barrier height and is inherent to all the existing barrier height calculation. However, we show in fig. 7 that it is possible to improve significantly the cross section calculation by introducing for each reaction a renormalization of the HFB energy surface by a deformation-independent parameter adjusted on experimental cross sections [68]. Some systematics can be deduced from such a renormalization procedure. An optimized fit within the $0.01 \leq E \leq 10$ MeV energy range is obtained with a constant renormalization factor amounting to 0.86, 0.89, 0.94 and 1.02 for nuclei with even-even, even-odd, odd-even and odd-odd numbers of protons and neutrons, respectively. Based on such a systematics, it can be seen in fig. 7 that the prediction of experimental data becomes rather satisfactory, at least in astrophysical standards, and of the same overall quality as the calculations performed with all

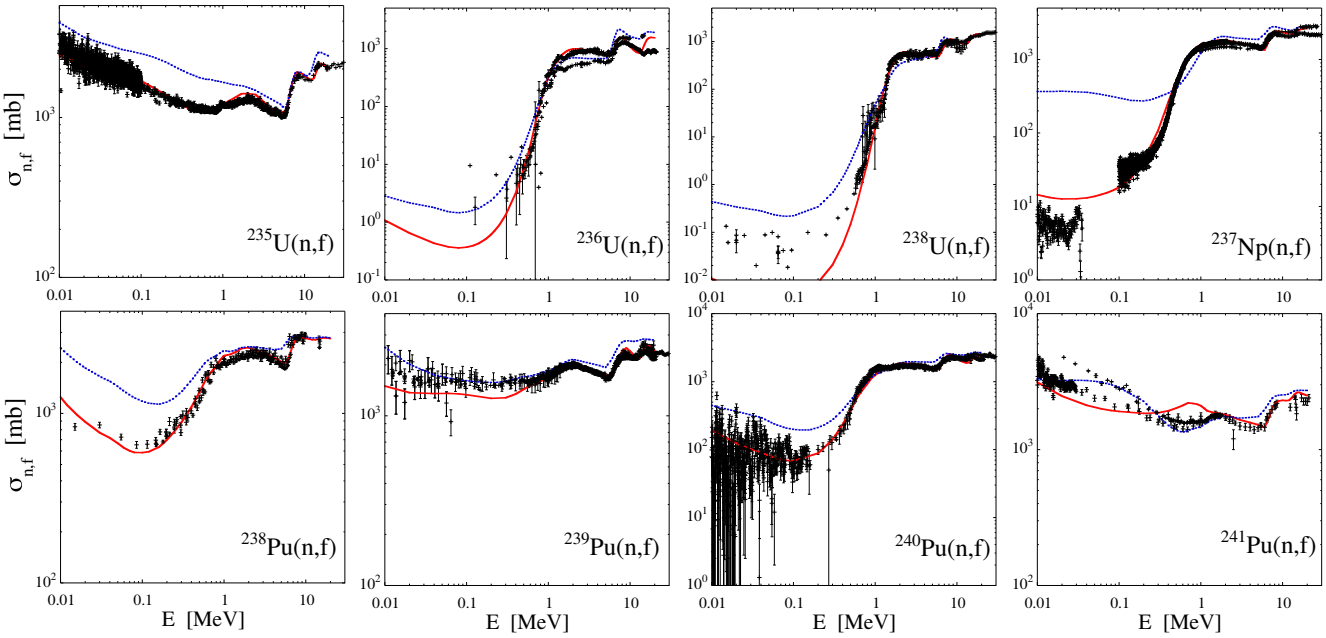

Fig. 7. Neutron-induced fission cross sections, for a sample of 8 actinides, obtained with the HFB fission path and HFB plus combinatorial NLD when the fission paths are renormalized by one optimized parameter for each nucleus (solid line) [68] or by the systematics given in the text (dotted line). Experimental data are taken from the EXFOR library [72].

the adjusted RIPL-3 recommendations [61]. The overall default deviation by a factor of more than 10 is reduced to less than a factor of 3. More details can be found in refs. [61,68]. Similar calculations based on the inverted parabola double-humped fission path and Fermi-gas–type NLD can be found in ref. [74].

Based on such a global renormalization procedure, all the neutron- and photo-induced reaction rates of astrophysical interest have been estimated for all nuclei with $90 \leq Z \leq 110$ from the valley of β-stability to the neutron drip line and can be found in a table and graphical format in the BRUSLIB library [45]. Similarly, the β-delayed and spontaneous fission rates have been estimated on the basis of the same fission barrier penetration calculation as predicted by the TALYS code [68]. The β-delayed fission rate is estimated taking into account the full competition between the fission, neutron and photon channels, weighted by the population probability given by the β-decay strength function, *i.e.*

$$\lambda_{\beta df} = \frac{(g_A/g_V)^2_{\rm eff}}{D} \int_{B_f}^{Q_\beta} \frac{\Gamma_f}{\Gamma_f + \Gamma_n + \Gamma_\gamma} S_\beta(E) f_0(Q_\beta - E) \mathrm{d}E, \quad (1)$$

where B_f is the fission barrier, Q_β the β-decay Q-value and S_β the β-decay strength function estimated within the Gross Theory [75]. For the phase space factor f_0, the factor D and the vector g_V and axial vector g_A coupling constants, we refer to ref. [76]. Γ_f, Γ_n, Γ_γ are the fission, neutron emission and electromagnetic de-excitation widths, respectively, at a given energy E which have been calculated consistently with the TALYS reaction code. Only few experimental data exist on β-delayed fission probabilities, especially on the neutron-rich side where the probability hardly exceeds some 10^{-5} [78]. In these circumstances, it remains difficult to test the predictive power of the theory, especially when so many nuclear ingredients come into play.

The spontaneous fission rate is deduced from the well-known formula $\lambda_{SF} = f_0 P$ where P is the barrier penetrability of the ground state calculated with the TALYS code and $f_0 = \omega_0/2\pi$ the frequency of oscillations in the fission mode for the ground state in the first well at the energy $\hbar\omega_0 \simeq 0.75$ MeV. It remains difficult to reproduce globally experimental spontaneous fission half-lives in the whole known region, *i.e.* on the proton- and neutron-rich sides of the valley of β-stability, as well as for the lightest very long-lived or the super-heavy nuclei. A modification of the fission barrier by typically 1 MeV can affect the half-live up to 9 orders of magnitude. As far as the r-process applications are concerned, spontaneous fission usually impact the abundances in a binary way, *i.e.* either the half-live is so long that it does not affect the decay or it is so fast that it drives the fission recycling, regardless of the other competing channels.

The main fission regions by one of these four fission processes are illustrated in fig. 8, when use is made of the above-mentioned nuclear inputs, in particular the HFB-14 fission paths (lower panel). Note that above $Z = 110$, HFB-14 model predicts low fission barriers and fission to dominate the decay of all neutron-rich nuclei [77]; the artificial $Z = 110$ limit is consequently an excellent approximation, as shown in ref. [77]. In order to perform sensitivity calculations, a similar calculation is made based on the MS99 fission barriers [64]. Since only primary barriers are available in this case, all the HFB-14 fission paths are scaled, so that for each nucleus the highest barrier

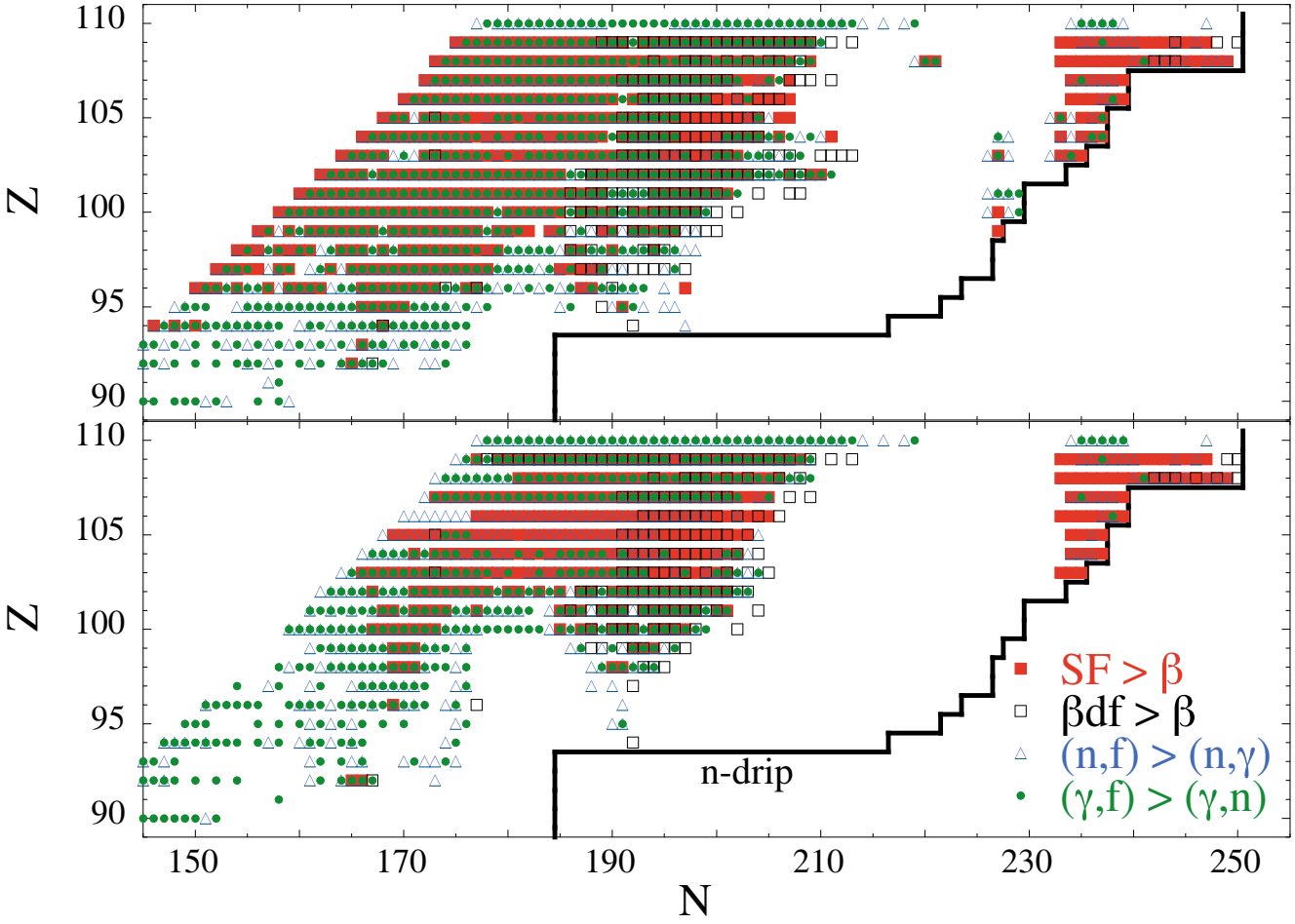

Fig. 8. (Color online) Representation of dominant fission regions in the (N, Z) plane. Nuclei for which spontaneous fission is estimated to be faster than β-decays are shown by full squares, those for which β-delayed fission is faster than β-decays by open squares, those for which neutron-induced fission is faster than radiative neutron capture at $T = 10^9$ K by open triangles and those for which photo-fission at $T = 10^9$ K is faster than photo-neutron emission by closed circles. The lower panel is obtained with the HFB-14 fission path, while the upper panel is derived assuming the fission paths are renormalized on the MS99 prediction [64]. For $Z > 110$, fission is found to dominate the decay mode [77].

corresponds now to the highest MS99 barrier [64]. The latter usually predicts lower barriers than the mean-field approach (see fig. 3), so that many more nuclei are found to be affected by fission processes when use is made of the MS99 barriers, as shown in fig. 8. Note that MS99 barriers may not always be available for very exotic n-rich nuclei close to the neutron drip line, especially for $Z \geq 106$. In this case, the HFB-14 barriers are adopted. This explains the relatively similar (and fast) fissioning region for $Z \geq 103$ at the neutron drip line (fig. 8; see also fig. 5).

3.4 Fission fragment distribution

The FFD plays a key role in nucleosynthesis simulations since it defines the light species that will be produced by the fission recycling (see sect. 4). Both the Z- and A-dependencies of the fragment distribution need to be determined for all potentially fissioning nucleus. Since the widely used Gaussian model of Kodoma and Takahashi [75], a number of new global scission-point models have recently been proposed and extended to exotic nuclei for astrophysical applications.

The first model considered here, the so-called SPY model, corresponds to a renewed statistical scission-point model based on microscopic ingredients [79]. The scission-point description is well suited to assess theoretically the energy distributions including kinetic, excitation, and available energy for each couple of primary fission fragments since their properties (mass, nuclear charge, ...) are fully defined at this point and do not evolve anymore. The main ingredient in the SPY model is the individual potential energy of each fission fragment as a function of its axial deformation. This quantity is estimated within the Gogny-HFB mean-field approach and is compiled in the AMEDEE database [80] for more than 8000 nuclei. Based on the assumption of a statistical equilibrium, the probability of a given fragmentation is related to its available state. Once the available energies are calculated for each fragmentation, a microcanonical

description including nuclear Fermi gas state densities is used to determine available phase space, hence the main fission fragment observables, more particularly mass and charge yields, kinetic energy and excitation energy of the fragments. The symmetric-asymmetric mass splitting is defined on the basis of a careful calculation of the available energy at scission. It was shown [79] that a detailed energy balance at scission, involving a complete microscopic description of the nuclear structure of the two fragments, is able to explain qualitatively the evolution from asymmetric to symmetric fragmentation for intermediate mass nuclei as well as heavy actinides. The number of evaporated neutrons is deduced from the mean excitation energy of each fragment.

The second model considered here is the phenomenological model GEF [81–83], which estimates the properties of the fission fragments and the emitted neutrons and photons in a global and semi-empirical way. The description of the fissioning system is based on the microscopic-macroscopic approach, where the microscopic properties are essentially determined by the shell effects of the fragments and only the macroscopic properties of the fissioning system are taken into account. The GEF model relies on an empirical description of the macroscopic stiffness parameters in the relevant normal modes and empirically derived fragment shells. The scission-point model is applied with inclusion of dynamical effects to include the impact of inertia along the fission trajectory. The influence of quantum mechanics, in particular the zero-point motion, is included to model the collective degree of freedom, which are treated as an harmonic quantum oscillator coupled to a heat bath. The parameters of the quantum oscillators are derived from experimental data. The yields of the different fission channels and their properties are attributed to the number of relevant states above the potential-energy landscape on the fission path at the moment of dynamical freeze-out. The excitation-energy-sorting mechanism determines the prompt neutron yields and the odd-even effect in fission-fragment yields of even-Z and odd-Z systems. The neutron evaporation is calculated with a Monte Carlo statistical approach using level densities from empirical systematics and binding energies with theoretical shell effects with gamma competition included. The GEF model has proven its capacity to describe experimental FFD extremely well, at the expense of introducing empirical adjustments. For this reason, the GEF predictions are originally restricted to nuclei which are not too neutron-rich, *i.e.* $A/Z < 2.8$ and $N < 170$. We took however the liberty to extend the predictions up to the neutron drip line. More details on the GEF model can be found in [81–83] and references therein.

Both the SPY and GEF models predict significantly different FFDs, as illustrated in fig. 9 where the mass yields of $A = 278$ isobars of particular relevance for the r-process (see sect. 4) are shown. In the GEF case, the fragment distribution are essentially symmetrical for these particular fissioning nuclei (except for $Z = 97$–99), whereas a 4-peak distribution is predicted by SPY for all the corresponding isobars. Similar patterns are seen both

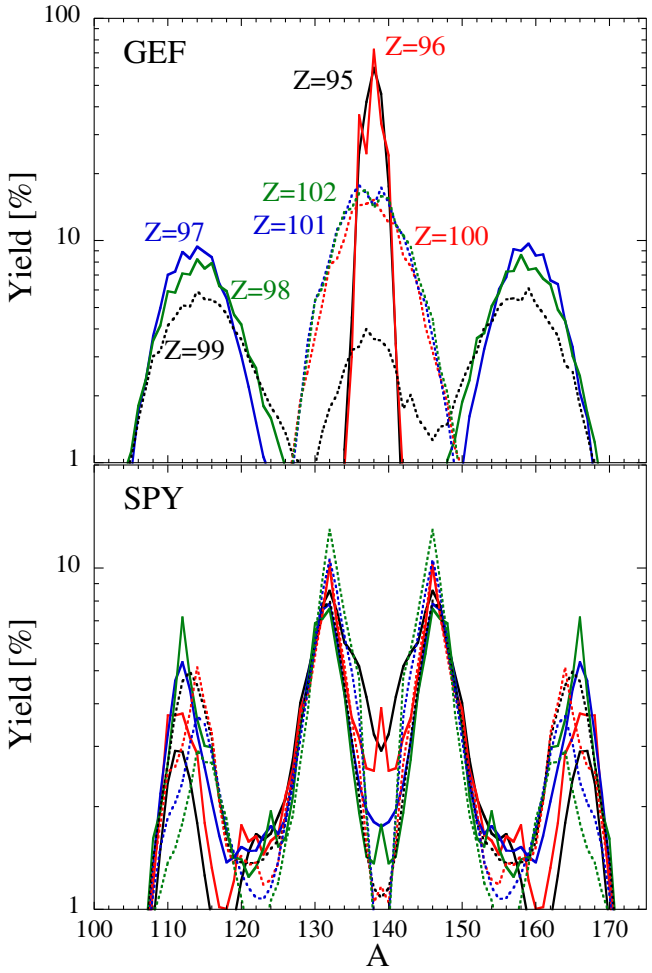

Fig. 9. (Color online) FFDs predicted by the GEF (upper panel) and SPY models (lower panel) for 8 $A = 278$ isobars. In the latter case, the 8 FFD have more or less the same 4-humped pattern.

in the mass distribution and in the charge distributions. During the neutron irradiation, elements down to Sr may be recycled from the fission. SPY doubly asymmetric fragment distributions can be traced back to the predicted Gogny-HFB potential energies at large deformations for the neutron-rich fragments favored by the $A \simeq 278$ fission [17]. Additional detailed Gogny-HFB calculations of the potential energy surface in the parent fissioning nucleus have confirmed qualitatively the theoretical prediction of these two asymmetric fission modes [17,84]. Such a new type of fission mode has however never been observed experimentally yet for experimentally accessible nuclei.

In fig. 10, we compare the SPY and GEF model predictions of the charge FFD for 5 neutron-rich isotopes of Hs ($Z = 108$) close to the neutron drip line. These nuclei are representative of the fissioning nuclei during the neutron irradiation (see sect. 4 and fig. 8). Significantly different distributions are observed with a smooth GEF asymmetric charge distribution, while the SPY model predicts either a symmetric ($A = 342$) or a triple-hump charge distribution ($A = 350$). Both distributions show that the fission

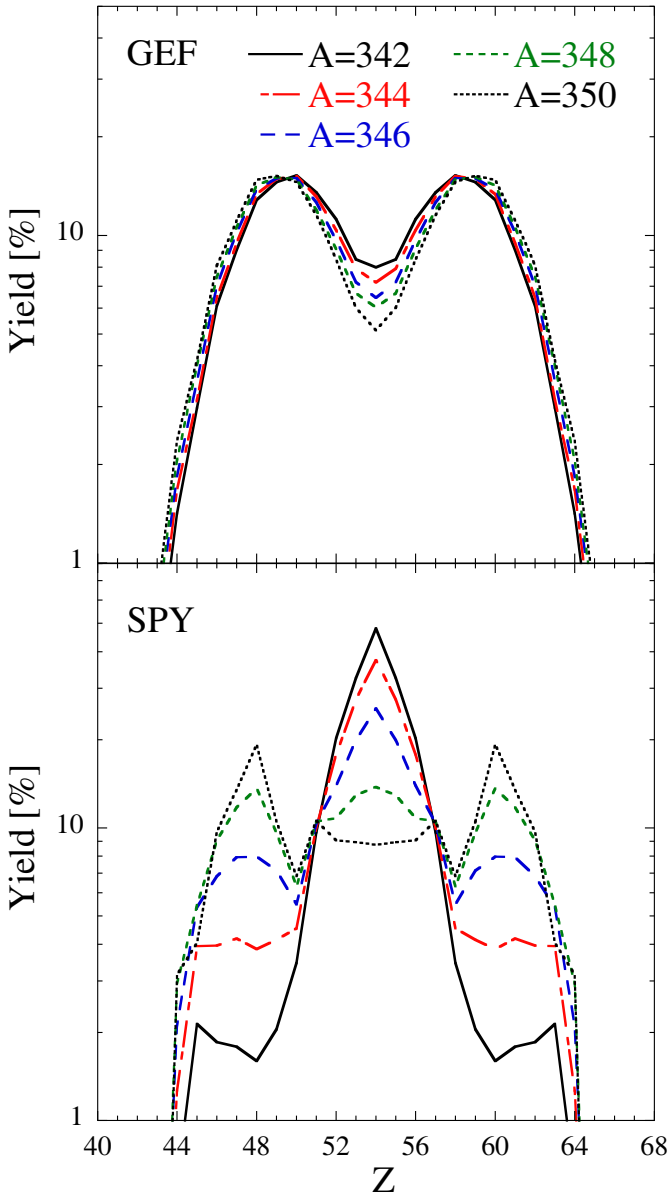

Fig. 10. (Color online) Charge FFDs predicted by the GEF (upper panel) and SPY models (lower panel) for 5 even-even neutron-rich isotopes of Hs ($Z = 108$) close to the neutron drip line.

recycling of such fissioning nuclei can produce elements as light as Ru to Cd, which have a neutron drip line predicted by the HFB mass models beyond the $N = 82$ shell closure. As a consequence, during the neutron irradiation, their fission recycling cannot contribute to a possible enrichment in the $N = 82$, $A = 130$ mass region corresponding to the second r-process peak, as discussed below.

Finally, we show in fig. 11 the SPY and GEF predictions of the average number of evaporated neutrons for each spontaneously fissioning nucleus. This average number is seen to reach, for both models, values of about four for the $A \simeq 278$ isobars and maximum values of ~ 14 for the heaviest $Z \simeq 110$ nuclei lying at the neutron drip line.

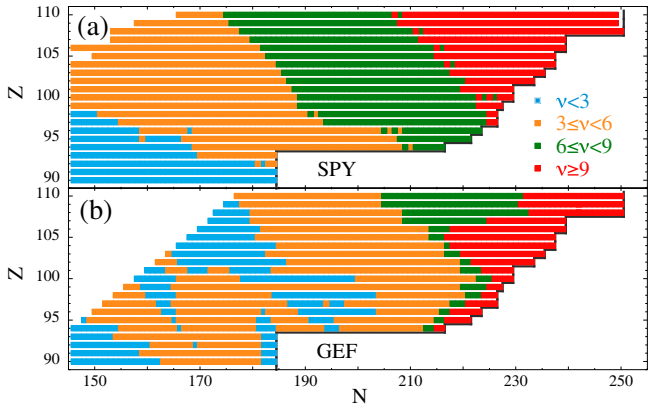

Fig. 11. (Color online) Representation in the (N, Z) plane of the average number ν of prompt neutrons predicted by the SPY (upper panel) and GEF (lower panel) models to be emitted from the ground state fission of a nucleus of charge Z and neutron number N.

4 Impact of fission on nucleosynthesis calculations

Based on the NS merger simulation and the r-process nucleosynthesis calculation, as described in sect. 2, it is possible to estimate the role of fission, at least in this specific r-process scenario. Due to the specific initial conditions of high neutron densities (typically $N_n \simeq 10^{33-35}\,\mathrm{cm}^{-3}$ at the drip density), the nuclear flow during most of the neutron irradiation will follow the neutron drip line and produce in tens of ms the heaviest drip-line nuclei (see upper panel of fig. 12). However, for drip-line nuclei with $Z \geq 103$, neutron-induced as well as spontaneous fission becomes efficient (at least according to the HFB-14 predictions, see fig. 8) prohibiting the formation of super-heavy nuclei and recycling the heavy material into lighter fragments which will restart capturing the free neutrons. For such heavy fissioning nuclei, the charge distribution of the fission fragments (see fig. 10) reaches elements typically above Ru ($Z = 44$) for which the neutron drip line is predicted by the HFB mass model to be beyond the $N = 82$ shell closure (see fig. 12). Due to the large neutron irradiation, all fission fragments re-capture neutrons bringing the nuclear flow back to the neutron drip line, so that the fission recycling of these $Z \gtrsim 103$ nuclei hardly contributes to a significant production of the second $N = 82$ r-process peak (see in particular the middle panel of fig. 12). Depending on the expansion velocity of the trajectory, fission recycling can take place two to three times before the neutrons are exhausted, as illustrated by the time evolution of the average mass number in fig. 13 for a given representative trajectory. During the irradiation time, the matter is heated by the radioactive decay of β-unstable nuclei, but also by the fission processes which provide first around 30% of the total heating rate at early times, as shown in fig. 14. After several hundred of ms, the density has dropped by a few orders of magnitude and the neutron density experiences a dramatic fall-off when neutrons get exhausted by captures. During this second phase

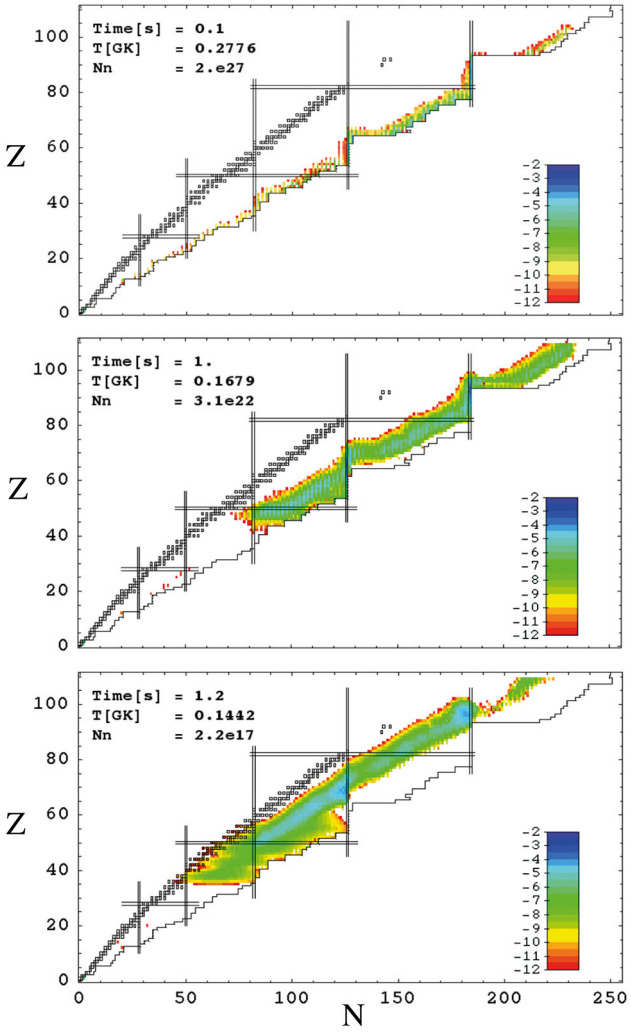

Fig. 12. (Color online) Representation in the (N, Z) plane of the r-process nuclear flow in a given mass elements ejected from the 1.35–1.35$M_\odot$ NS merger. The nuclear flow is colour coded in terms of the mass fraction of nuclei (in log scale) at three different times: 0.1 s (upper panel), 1 s (middle panel) and 1.2 s (lower panel) after ejection. The corresponding temperature T (in GK) and the neutron density N_n (in cm^{-3}) are also given in the panels. The open squares depict the valley of β-stability, the double lines the neutron and proton magic numbers and the solid line the HFB-21 neutron drip line.

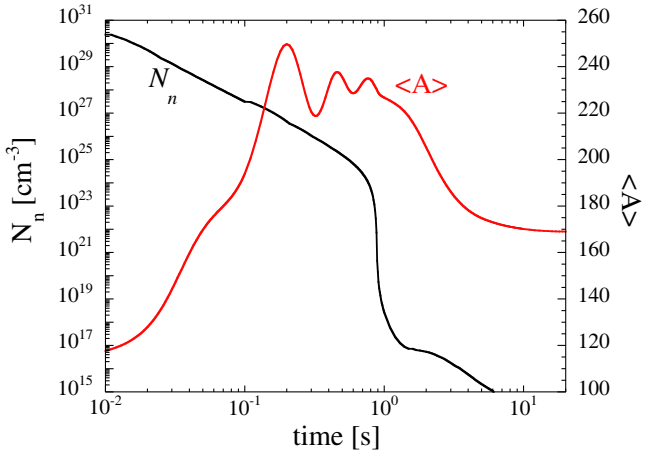

Fig. 13. (Color online) time evolution of the neutron density N_n and average mass number $\langle A \rangle$ for a specific representative mass element ejected from the 1.35–1.35$M_\odot$ NS merger.

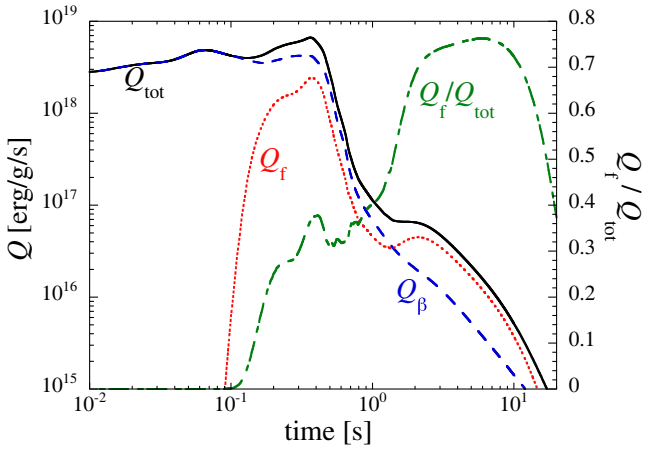

Fig. 14. (Color online) time evolution of the total mass-averaged radioactive heating rate per unit mass $Q_{\rm tot}$ (black solid line) and its β-decay Q_β (dashed line) and fission $Q_{\rm f}$ (dotted line) contributions for the matter ejected from the 1.35–1.35$M_\odot$ NS merger. The $Q_{\rm f}/Q_{\rm tot}$ ratio is also given (dash-dotted line; right axis).

(see middle and lower panels of fig. 12), the nuclear flow around the $N = 126$ and $N = 184$ regions follows the isotonic chains. When the neutron density reaches some $N_n = 10^{20}$ cm^{-3}, the timescale of neutron capture for the most abundant $N = 126$ and $N = 184$ nuclei becomes larger than a few seconds, and the nuclear flow is dominated by β-decays back to the stability line (as well as fission and α-decay for the heaviest species). During this phase, the heating rate is dominated by the fission processes, mainly β-delayed fission and spontaneous (fig. 14). Note that photo-fission rarely plays a key role, except for a few specific trajectories which are still hot enough at the time fission takes place, *i.e.* after a few hundreds of ms.

The final composition of the ejecta during the neutron star merging is shown in fig. 15. This distribution is found to be insensitive to many astrophysical conditions, in particular the initial abundances, the NS masses, the quantity of matter ejected or the EOS [16]. This robustness, which is compatible with the uniform, solar-like abundance pattern of the elements observed in metal-poor stars [27–29], is linked to the fission recycling. In contrast, the distribution is rather sensitive to the adopted nuclear models, as summarized in fig. 16 and detailed in the present section. Our standard case shown in fig. 15 is obtained with the nuclear models described in sect. 2, including in particular the fission rates based on the HFB-14 fission paths and the FFDs and average number of prompt neutrons predicted by the SPY scission model.

The $A = 195$ abundance peak related to the $N = 126$ shell closure is found to be produced in solar proportion

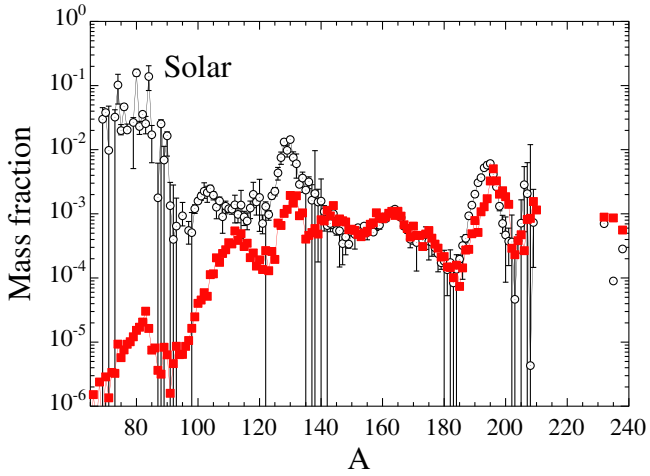

Fig. 15. (Color online) Final abundance distribution of the matter ejected from the 1.35–1.35$M_\odot$ NS merger as a function of the atomic mass. The distribution is compared with the solar r-abundance distribution [85] (dotted circles). All nuclei above Bi are assumed to have decayed except ^{235,238}U and ^{232}Th.

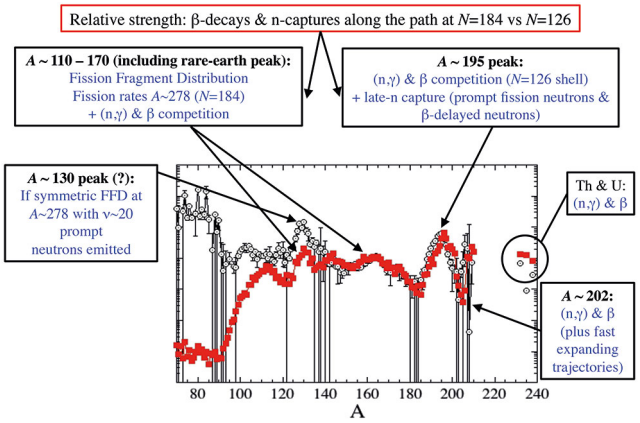

Fig. 16. (Color online) Schematic representation on the way the nuclear input influences the calculated r-process abundances in the different mass regions. For each region, the main nuclear ingredients affecting the predictions are given. See text for more details.

and not to be too sensitive to the fission model (except through the capture of late neutrons emitted by fission or β-delayed processes, see sect. 4.2), but rather sensitive to the competition between the radiative neutron captures and β-decays along the $N = 126$ isotonic chain. In contrast, the $110 \lesssim A \lesssim 170$ nuclei originates exclusively from the fission recycling, which takes place in the $A \simeq 278$ region at the time all neutrons have been captured and the β-decays dominate the nuclear flow. The $A \simeq 278$ isobar corresponds to the predominant abundance peak in the actinide region during the irradiation phase due to the turn-off point at the $N = 184$ drip-line shell closure, as shown in the lower panel of fig. 12. The nuclei that β-decay along the $A \simeq 278$ isobar fission asymmetrically according to the SPY FFD model, as shown in fig. 9, leading to the four-hump pattern seen in figs. 15 and 16. The abundance strength in this $110 \lesssim A \lesssim 170$ region relative to the $A \simeq 195$ peak depends in turn on the accumulation of matter along the $N = 184$ and $N = 126$ r-process path and consequently on the neutron captures and β-decays taking place at these neutron shell closures. As discussed in sect. 4.2, would 15 to 20 neutrons be emitted per fissioning nuclei and the FFD for the $A \simeq 278$ nuclei be strongly symmetrically peaked, the second r-process peak could be produced by fission recycling (see sect. 4.1). These conditions seem, however, not to be predicted by the most sophisticated non-phenomenological models.

In contrast to the other regions, the production in the $A \simeq 202$ trough is sensitive to the competition between the neutron captures and β-decays, but also to the dynamics of the ejection [86,87]. Indeed, in relativistic hydrodynamic simulations, some mass elements are found to be ejected at high velocities, so that these fast expanding mass elements might not have time to capture all available free neutrons leading to no or only one fission cycle. Though the integrated mass associated with a fast expansion remains small relative to the slowly expanding ones, their contributions to the final abundance distribution are found to be non-negligible, in particular around $A \simeq 200$, where their high abundances tend to fill the trough found in slowly expanding trajectories. For this reason, the Newtonian description of the NS merger hydrodynamics [25] which tends to predict rather slower expansions with respect to relativistic simulations (see discussion in ref. [16]) may give rise to different nucleosynthesis predictions in this region. Note that the Newtonian simulations also present the drawback of overestimating the ejecta mass in general, as discussed in refs. [11,16,25].

Finally, in the present calculation, super-heavy nuclei with $Z > 110$ cannot be produced due to the island of fissioning nuclei close to the neutron drip line (fig. 8). This unstable region with respect to fission is found with the HFB-14 barriers. None of the other barrier compilations include these neutron-rich nuclei, so that at this stage it cannot be confirmed that the super-heavies close to $N \simeq 250$ could not be produced. Would the fission barriers be larger, the nuclear flow could reach the next $N \simeq 256$ shell closure and pile up in this region before fissioning. In this case, the α-, β-decays as well as the fission of $A \simeq 380$ nuclei could potentially be at the origin of super-heavy long-lived nuclei, if any, and also affect the final r-abundance distribution [77,88]. However, there is no calculation up to now that could confirm the production of such species by the r-process.

4.1 Impact of the fission barrier height and FFD

As explained in sect. 3, two sets of fission barriers are considered in the present analysis, namely the HFB-14 and the MS99 barriers. Note that in the MS99 model, the barrier height is used to renormalize each fission path obtained within the HFB-14 framework, but the NLD are kept identical. The impact of the adopted fission model is shown in fig. 17 where the r-abundance distribution are

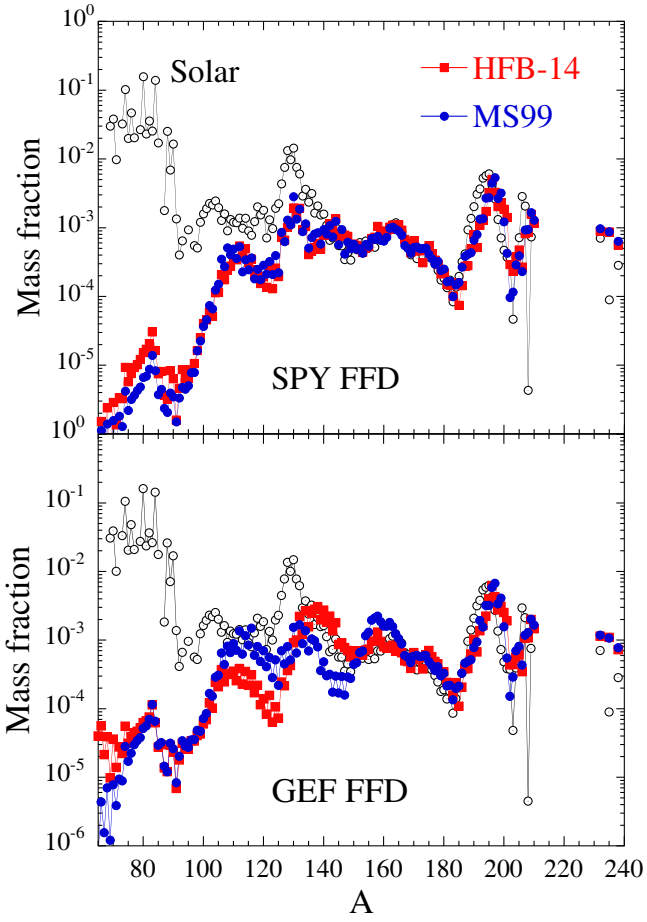

Fig. 17. (Color online) The same as fig. 15, where the squares correspond to the r-abundance distribution obtained with the HFB-14 fission path and corresponding fission rates and the circles with the fission path renormalized on the MS99 fission barriers. The SPY FFDs are used for the distributions of the upper panel and the GEF FFDs for the lower panel.

obtained with both fission models, but also with two distinct FFDs. In the upper panel, *i.e.* with the SPY FFDs, both abundance distributions are rather similar, whereas, in the lower panel with the GEF FFDs, significant differences are found. As explained above, the $110 \lesssim A \lesssim 170$ abundances originate essentially from the fission of the nuclei that β-decay at the end of the neutron irradiation and that were produced along the $N = 184$ shell closure. In particular, the $A \simeq 278$ nuclei with $N = 184$ correspond to the most abundant species produced during the neutron irradiation due to the bottleneck created by β-decays along the nuclear flow. When decaying back to the valley of stability, the fissioning nuclei first encountered along the $A = 278$ nuclear flow are predicted to be the $Z \simeq 101$–102 elements when considering the HFB-14 model and $Z \simeq 99$ with MS99 barriers (see fig. 8). Both regions are found to fission with the same doubly asymmetric mode according to the SPY model (see the rather similar FFDs in fig. 9) leading to similar r-abundance distributions (with a similar 4-hump pattern), as shown in the upper panel of fig. 17. In contrast, the GEF model

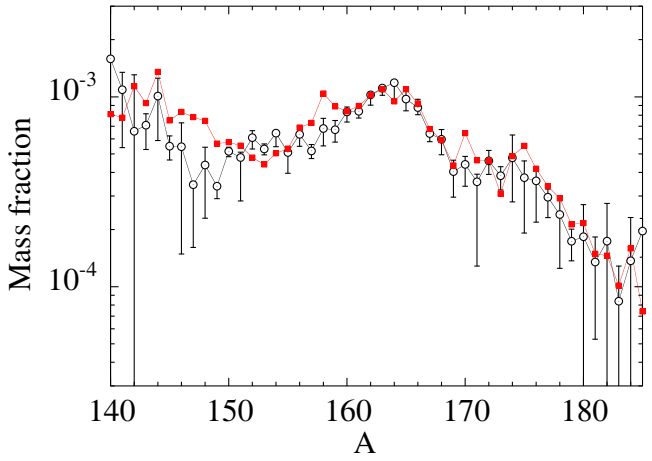

Fig. 18. (Color online) Comparison between the abundance distribution in the rare-earth region ($140 \leq A \leq 185$) ejected from the 1.35–1.35$M_\odot$ NS merger with the solar distribution. The calculated distribution is obtained with the HFB-14 fission path and corresponding fission rates and the SPY FFDs.

finds that ^{278}Es ($Z = 99$) fissions asymmetrically with a triple-hump pattern, while ^{278}Md ($Z = 101$) and ^{278}No ($Z = 102$) fission symmetrically (fig. 9). The corresponding symmetric fission gives rise to the $A \simeq 140$ abundance peak in fig. 17 (lower panel) with the HFB-14 barriers while the more pronounced triple-hump pattern can be observed if use is made of the MS99 barriers. As shown in fig. 18, the solar rare-earth peak around $A \simeq 165$ can be nicely explained thanks to the SPY prediction of the FFDs, and more particularly its doubly asymmetric fission mode [17]. Freeze-out effects through the late capture of fission neutrons also contribute to the final shaping of the rare-earth nuclides, as discussed in sect. 4.2. This scenario thus offers a consistent picture of the formation of the rare-earth elements within an r-process scenario, as initially suggested in ref. [89], different from alternative suggestions for the still obscure production of these elements, for example based on the freeze-out conditions in artificially high-entropy neutrino-driven winds [90] with all their associated astrophysical uncertainties [1–3].

This comparison shows that the final r-abundance distribution remains very sensitive to the fission barrier heights and FFDs. It is consequently of prime importance to determine both quantities on the basis of sound and as microscopic as possible physical models. In particular, Gaussian-type parametrisations of the FFD where the mass numbers and charges of the two main fragments are determined from extrapolation of systematics or empirical models (as given for example in refs. [75,91]) should be avoided, since they could give rise to any kind of final abundance predictions for $110 \leq A \leq 170$ production. This is illustrated in fig. 19, where the abundance distributions resulting from three different prescriptions for the FFD are shown. These include the two-Gaussian parametrisation of ref. [75], the five-Gaussian fit to chain yields [92] extrapolated to neutron-rich nuclei and the strongly peaked symmetric fission assuming all nuclei with

$A \geq 257$ spontaneously fission. While in the first two cases the HFB-14 fission paths are considered to estimate the fission rates, in the latter case, we have considered that all exotic neutron-rich nuclei with $A \geq 257$ fission, as sometimes assumed [93], in a first approximation, from the analysis of thermonuclear explosions that took place in the 1950s [94]. The two-Gaussian approximation [75] corresponds to an asymmetric distribution where the light and heavy main fragments are relatively close to each other, leading to a wide distribution around $A \simeq 140$. A modification of the mass number of the main mass fragments would have a direct impact on the r-abundance distribution. For example, if we assume a purely symmetric fission taking place around $A = 257$, a strong single peak emerges around $A = 130$ in the r-abundance distribution (fig. 19). Although this type of FFD describes relatively well the $A \geq 130$ solar distribution, there is no physical reason to justify such a FFD or that all nuclei with $A \geq 257$ fission (the conditions found in thermonuclear explosions being fundamentally different than in NS mergers). In contrast, the IAEA systematics [92] give rise to an extremely spread FFD leading to a flat abundance distribution and a relatively weak $A \simeq 195$ peak. These examples show that extrapolating experimentally based systematics can give rise to any possible r-process distribution in the $110 \leq A \leq 170$ region. Reproducing experimental FFD is a necessary condition, but definitely not a sufficient one when applying a given model to r-process applications. FFD distributions should definitely not be blindly extrapolated from systematics on experimentally known nuclei and even less tuned in order to reproduce at best the solar system distribution, a strategy which is sometimes followed when dealing with r-process calculations [91].

4.2 Impact of prompt neutron emission

If the fission process is followed by the emission of prompt neutrons, the final r-abundance distribution may be affected in a non-negligible way, in particular at freeze-out, when most of the free neutrons have been captured. According to both the SPY and GEF models, the fission of the most abundant nuclei around $A = 278$ is accompanied with the emission of typically 3 to 4 neutrons (fig. 11). Adding to the neutrons emitted by β-delayed processes, these late fission neutrons can represent up to 80% of the neutrons emitted when the nuclear flow decays back to the valley of stability and are found to be dominantly recaptured by the abundant nuclei forming the $N = 126$ peak. For this reason, not only the abundance distribution for $A \lesssim 170$ is slightly shifted to lower masses by a few units, but the $A = 196$ peak which recaptures the emitted free neutrons is shifted to higher masses, as shown in figs. 20 and 21.

In contrast, if we artificially assume that each fissioning process leads to the emission of about 20 neutrons (corresponding to the upper limits found by some models [91]), the same mechanism is found but to a much larger extent. In particular, the $A = 196$ peak is shifted

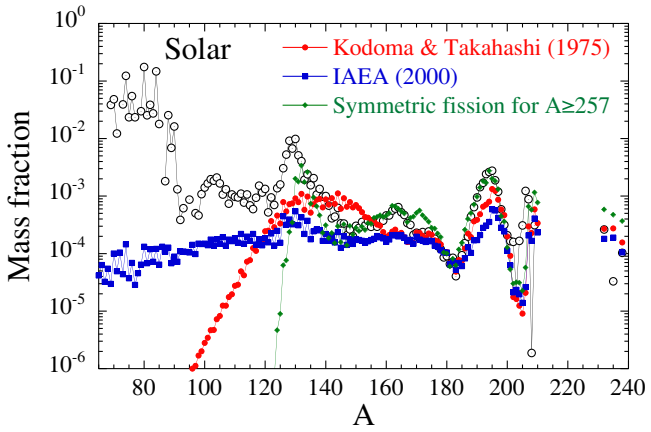

Fig. 19. (Color online) The same as fig. 15, where the r-abundance distribution are calculated with the FFDs derived from phenomenological prescriptions, such as the Kodoma and Takahashi (1975) model [75], the IAEA systematics [92] or an adjusted symmetric FFD assuming in addition all nuclei above $A = 257$ fission spontaneously (see text for more details).

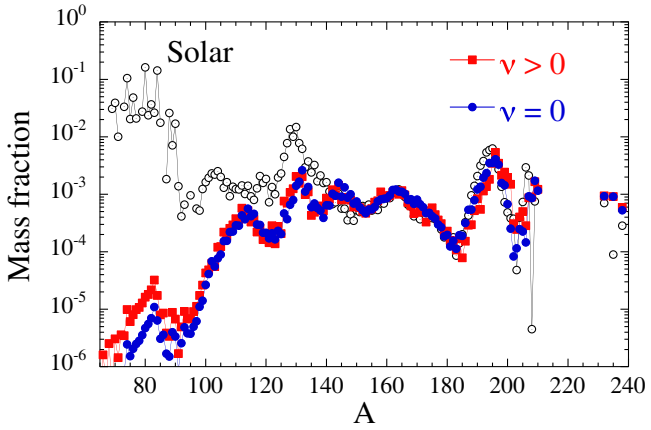

Fig. 20. (Color online) The same as fig. 15, where the squares correspond to the r-abundance distribution obtained with the SPY FFDs with prompt neutron emission (see fig. 11) and the circles without neutron emission ($\nu = 0$).

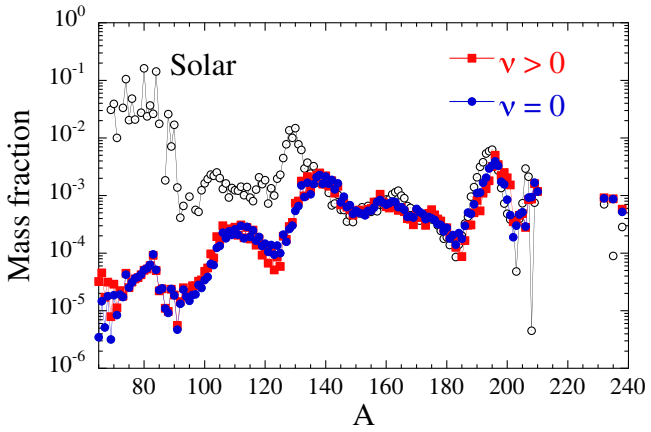

Fig. 21. (Color online) The same as fig. 15, where the squares correspond to the r-abundance distribution obtained with the GEF FFD with prompt neutron emission (see fig. 11) and the circles without neutron emission ($\nu = 0$).

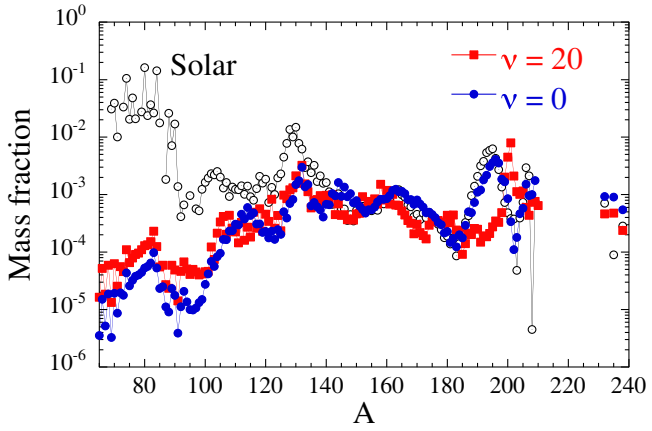

Fig. 22. (Color online) The same as fig. 15, where the circles correspond to the r-abundance distribution obtained with the SPY FFD without prompt neutron emission and the squares assuming each fission process leads to the emission of $\nu = 20$ prompt neutrons.

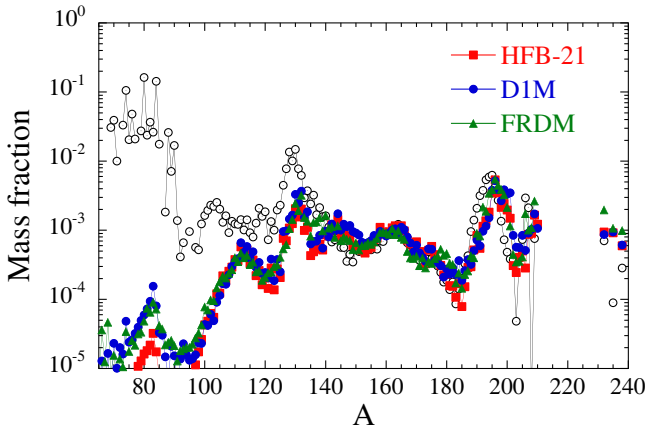

Fig. 23. Abundance distribution of the matter ejected from the 1.35–1.35$M_\odot$ NS merger obtained with reaction rates calculated either with HFB-21 [49], D1M [96] or FRDM [97] masses.

to $A \simeq 201$ and found to be much narrower due to its formation at later times (typically 1 sec after the start of the r-process) when the prompt neutrons are emitted and the temperature is rather low. As long as free neutrons are produced, the neutron density $N_n \simeq 10^{18}\,\mathrm{cm}^{-3}$ is maintained during a few fractions of a second and reshapes the abundance distribution as shown in fig. 22. Would the $A \simeq 278$ nuclei fission symmetrically, with such a high number of prompt neutrons emitted, the main fission products would peak around $A = 129$ and the second r-process peak at $A = 130$ could be produced in significant amount. There is however no reasonable FFD model predicting that so many neutrons would be emitted by the fission of $A \simeq 278$ nuclei and that the corresponding fission mode is purely symmetric.

The late re-capture of this fission neutron clearly affects the predicted abundances. The final r-abundance distribution remains therefore rather sensitive to the number of prompt neutrons emitted by fission processes. It is consequently of prime importance to determine this quantity from sound physical models (such as GEF and SPY) rather than to use extrapolations from systematics derived from the few experimental data available [91].

5 Uncertainties associated with neutron capture and β-decay rates

The global abundance pattern discussed in the previous section can also be affected by the still uncertain neutron-capture and β-decay rates, as already discussed in refs. [17, 95]. In the present section, we briefly study the way the neutron-capture and β-decay rates affect the abundance distribution, and to what extent they can modify the conclusions drawn in sect. 4

5.1 Neutron-capture rates

During the decompression of the NS matter, the r-process dominantly takes place at low temperatures (below typically 1GK), so that the radiative neutron capture is in competition with β-decays rather than with the photodisintegrations, as traditionally found in hot environments like in the ν-driven wind [1]. Reaction rates therefore fully enter the reaction network.

Neutron capture rates can be affected by the still unknown nuclear inputs to the reaction model, as well as, more fundamentally, by the description of the reaction mechanism that is at stake for exotic neutron-rich nuclei. Among the various nuclear ingredients, nuclear masses are known to be of fundamental importance for the estimate of neutron capture rates. They define the reaction Q-values and consequently strongly affect the corresponding rates. We study here the sensitivity of the nucleosynthesis calculation by considering the TALYS neutron capture rates estimated with three different sets of nuclear masses, namely HFB-21 masses based on the Skyrme-HFB model [49], D1M masses based on the Gogny-HFB model [96] and the macroscopic-microscopic finite range droplet model (FRDM) [97]. The corresponding rates include a compound and a pre-equilibrium component but no direct capture (DC) contribution (see below). Deviations up to a factor of 10^7 can be found for drip line nuclei. However, such differences are seen in fig. 23 to have a rather small impact on the calculated r-abundances, deviations being restricted to the $A \simeq 180$ and $A \simeq 200$ regions. Note that the same β-decay rates [50] have been used in the nucleosynthesis calculations. Rather similar abundance distributions can be explained by the mass-averaging due to the large number of contributing trajectories, but also to the fact that the final distribution is shaped by the competition between neutron capture and β-decay for nuclei relatively close to the valley of β-stability at the time of the neutron freeze-out (see ref. [1] for more details). Despite this similarity, more work on nuclear masses and all the relevant nuclear inputs to the reaction model (*i.e.* also nuclear level densities, gamma-ray strength, optical potential, ...) [48] is obviously needed, in particular to improve the prediction around the $A \simeq 195$ peak.

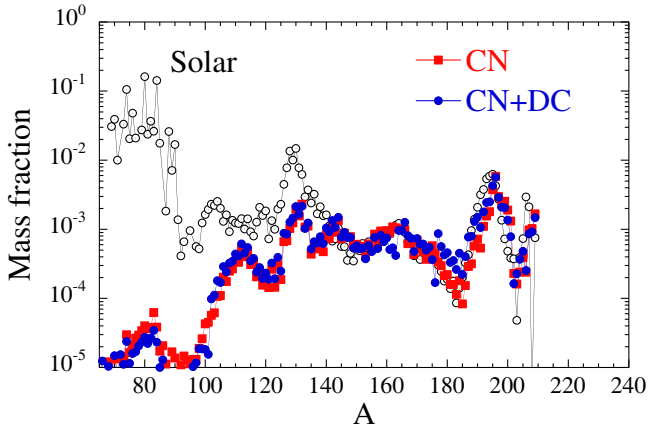

Fig. 24. (Color online) Abundance distribution of the matter ejected from the 1.35–1.35$M_\odot$ NS merger obtained with reaction rates calculated either in the CN statistical model or when both the CN and DC contributions are included.

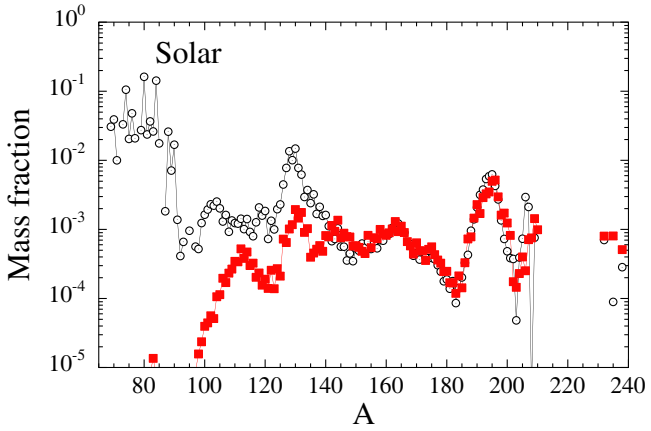

Fig. 25. (Color online) The same as fig. 15 where the HFB-21+GT2 β-decay rates for the seven $N = 126$ isotopes with $A = 188$–195 (*i.e.* $Z = 62$–69) are artificially reduced by a factor of 2.

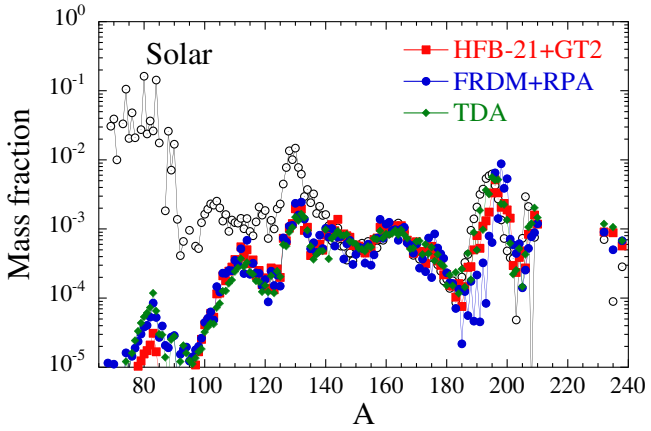

Fig. 26. (Color online) The same as fig. 15 but with abundance distributions obtained with three different models of β-decay rates, the HFB21-GT2 [50], the FRDM+RPA [102] and the Tamm-Dancoff approximation (TDA) [103]

Concerning the reaction mechanism, when the number of available states in the compound nucleus (CN) is relatively small, the capture reaction is known to be possibly dominated by direct electromagnetic transitions to a bound final state rather than through a compound nucleus intermediary. This DC proceeds via the excitation of only a few degrees of freedom on much shorter time scale reflecting the time taken by the projectile to travel across the target. This mechanism can be satisfactorily described with the perturbative approach known as the potential model [98–101]. It is now well accepted that the DC is important, and often dominant at the very low energies of astrophysical interest for light or exotic nuclei systems for which few, or even no resonant states are available. The direct contribution to the neutron capture rate can be 2 to 3 orders of magnitude larger than the one obtained within the Hauser-Feshbach approach classically used in nucleosynthesis applications. The impact on $170 \leq A \leq 200$ abundances is seen in fig. 24 to be non-negligible, but the global distribution remains rather similar. Further improvements of the nuclear ingredients required for a proper description of the DC cross section, *i.e.* mainly the optical potential and spectroscopic factors in addition to the nuclear structure properties, is needed, especially for exotic neutron-rich nuclei. More details can be found in ref. [101].

5.2 β-decay rates

As illustrated in fig. 16, the relative strength of the $A = 195$ third r-process peak and the overall recycled material in the $110 \leq A \leq 170$ range is linked to the amount of material accumulated in the bottleneck at the $N = 126$ and $N = 184$ shell closures, respectively. In particular, the height of the third r-process peak is affected by the absolute value of the β-decay rates around the $N = 126$ isotonic chain, since the slow β-decay sets the timescales for the production of heavy nuclei during the expansion of the material. As a sensitivity test, we show in fig. 25 our standard calculation based on the HFB-14 fission path and the SPY FFD (fig. 15), but with β-decay rates for the eight $N = 126$ isotopes with $A = 188$–195 (*i.e.* $Z = 62$–69) smaller by a factor of 2. This reduction factor is well within the uncertainty affecting the β-decay prediction of exotic neutron-rich nuclei (though it will need to be confirmed), and is shown to affect directly the production of the $A = 188$–195 isobaric r-elements, which show now an abundance pattern much closer to the solar system distribution.

Similarly, fig. 26 shows the predicted abundance distributions obtained with three sets of β-decay rates, namely the HFB21-GT2 [50], the FRDM+RPA [102] and the Tamm-Dancoff approximation (TDA) [103]. The different rates are seen to affect essentially the third r-process peak which can be shifted or present odd-even effects, but the impact on the $110 \leq A \leq 170$ abundances remains rather limited. In particular, the production of the rare-earth elements remains qualitatively rather robust, as already pointed out [17].

Here also, guided by recent and future experiments on exotic neutron-rich nuclei, more theoretical effort needs to be devoted to improve the prediction of β-decay rates [104–106] in order to understand the production of this third r-process peak in solar proportion.

6 Production of the Th and U cosmochronometers

Some of the heaviest long-lived radioactive nuclei produced by the r-process can be used as nucleocosmochronometers [1]. In particular the abundance ratios of Th to Eu and Th to U have been proposed for estimating the age of the oldest stars in our galaxy. More specifically, a simple comparison of the observed abundance ratio with the production ratio can provide a stellar age estimate assuming the low-metallicity star has been polluted by a few r-process events only and the r-process is rather universal [27,107,108].

For ages longer than the half-life of Th progenitor nuclei, *i.e.* typically hundred Myr, the Th to Eu chronometry relates the star age T_* to the Th abundances through the expression

$$\left(\frac{\mathrm{Th}}{\mathrm{Eu}}\right)_{obs} = \left(\frac{\mathrm{Th}}{\mathrm{Eu}}\right)_{r} \exp\left[-T_*/\tau(\mathrm{Th})\right], \qquad (2)$$

where $\tau(\mathrm{Th}) = 20.27\,\mathrm{Gy}$ is the characteristic α-decay timescale of Th and the subscripts *obs* and *r* refer to the observed and r-process abundance ratios, respectively. From eq. (2), it can be seen that the Th/Eu abundance has to be determined within less than 16% if we hope to predict the stellar age within less than 3 Gy. The r-process production of Eu and Th is obviously model dependent and can in addition be strongly affected by uncertainties in the description of the fission process, as shown, for example, in fig. 18.

Among the various chronometric pairs, the ^{232}Th to ^{238}U ratio has been shown to be relatively robust, in particular in comparison with the Th/Eu chronometry, *i.e.* to be less affected by the still large astrophysics and nuclear physics uncertainties affecting our understanding of the r-process nucleosynthesis [107,108]. This property is principally bound to the fact that Th and U are neighbour nuclei, and consequently their production ratio is not strongly affected by unreliable extrapolation procedures, but rather by local nuclear uncertainties, such as nuclear masses or fission processes in the actinide region. If Th and U lines are observed accurately and simultaneously in metal-poor stars, an age estimate could be derived from the expression

$$\log\left(\frac{\mathrm{Th}}{\mathrm{U}}\right)_{obs} = \log\left(\frac{\mathrm{Th}}{\mathrm{U}}\right)_{r} + \log \mathrm{e}\,\left(\frac{1}{\tau(\mathrm{U})} - \frac{1}{\tau(\mathrm{Th})}\right)\,T_*, \qquad (3)$$

where $\tau(\mathrm{U}) = 6.41\,\mathrm{Gy}$ is the characteristic α-decay timescale of U (this expression also assumes that all Th and U progenitors had time to decay, or in other words that the star is older than typically hundred My). From eq. (3), it is found that a ± 0.1 error on the observed or predicted production ratio, log(Th/U), gives rise to a ± 2.1 Gy error on T_* or equivalently the Th/U abundance has to be determined within less than 38% to predict the age of a star within less than 3 Gy.

For the various simulations performed in the present study, where only modifications of the fission probabilities and fragment distributions are considered, we find the ^{232}Th to ^{238}U production ratio to lie between 1.44 and 1.78. This allows us to estimate the age of very metal-poor stars for which both the Th and U lines have been clearly detected and the elemental abundances accurately determined. This is the case of the CS31082-001 star [107] the age of which can be estimated to 16.0 ± 1.0 Gy, adopting the observed abundance ratio of $\log(\mathrm{Th/U})_{obs} = 0.94 \pm 0.09$ [107,108]. The largest age of 17 Gy is obtained when use is made of the ETFSI fission barriers and GEF FFDs, while the smallest estimate of 15 Gy is found with the use of the HFB-14 fission path and the SPY FFDs. The fission model is consequently found to have a modest impact on the production of these actinides, but it cannot be excluded that future improved fission models give rise to rather different predictions. In contrast, different neutron capture rates can more significantly affect the production of Th and U, as shown in fig. 23, and consequently give rise to larger uncertainties on the age determination.

7 Conclusion

Decompressed matter from binary NS mergers remains a viable site for the r-process, which is extremely robust with respect to many astrophysical uncertainties. This robustness, which is compatible with the unique, solar-like abundance pattern of the elements heavier than Ba observed in metal-poor stars, supports the possible creation of these elements by fission recycling in NS merger ejecta. However, the estimated abundance distribution remains rather sensitive to the adopted nuclear models. The material ejected from the dynamical merging phase is composed almost exclusively of $A > 140$ nuclei, and in particular the $A \simeq 195$ third r-process peak appears in proportions similar to those observed in the solar system, deviations resulting essentially from the still difficult task to predict neutron capture and β-decay rates, as well as the number of prompt fission neutrons emitted for exotic neutron-rich nuclei. The situation for the lightest $110 \lesssim A \lesssim 170$ species has been rather unclear up to now and extremely dependent on fission properties, including in particular the fission barriers and FFD. The abundance of $110 \lesssim A \lesssim 170$ nuclei is found to depend sensitively on the fission processes affecting the isobaric chains around $A \simeq 278$ at the end of the neutron irradiation when the abundant $N = 184$ nuclei decay back to the valley of stability. Both the fission probabilities and FFDs of nuclei in this region play a crucial role in shaping the production of

$110 \lesssim A \lesssim 170$ nuclei. Similarly, the production of superheavy nuclei during the neutron irradiation depends on the fission properties of nuclei with typically $Z \gtrsim 105$ at the neutron drip line. For these reason, fission properties need to be determined on the basis of sound and as microscopic as possible nuclear models. Phenomenological, empirical or systematics extrapolations in the exotic neutron-rich region should be avoided because of their lack of predictive power. Such models could lead to any possible final r-abundance pattern. In contrast, more work within microscopic approaches should be devoted to estimate fission paths and NLD at the fission saddle points to improve our predictions of the neutron-induced, β-delayed, spontaneous fission rates and fission yields, as much as possible within one unique consistent framework. Mean-field model calculations are now available and can be used to estimate the potential energy surfaces and associated collective inertia tensors for a microscopic analysis of the collective dynamics in low-energy fission through a study of the time evolution of the compound system on the basis of a time-dependent Schrödinger equation [84,109–112]. Such state-of-the-art approach has shown its ability to reproduce several important features of fission, including the fragment kinetic energy and mass distributions [111,112]. Moreover new breakthroughs have recently been done [113] to describe low-energy fission up to a few MeV above the fission barrier, where statistical models cannot be applied to treat the excitation energy. This so-called Schrödinger Collective Intrinsic Model may improve the existing microscopic models by taking the particle-vibration couplings into account. Indeed such model is able to describe the couplings of the individuals degrees of freedom to the nucleons collective motion in a fully microscopic and quantum mechanical way, without any other phenomenological parameters than the ones included in the effective nucleon-nucleon interaction.

Similarly, the FFD and the average number of emitted neutrons need to be determined on the basis of sound microscopic models since these ingredients directly influence the calculated abundance distribution. The unexpected doubly asymmetric FFD predicted by SPY also opens new perspectives in theoretical and experimental nuclear physics concerning specific fission modes related to the nuclear structure properties of exotic nuclei. Dynamical mean-field calculations based on the time-dependent generalized coordinate method [109–111] should quantitatively confirm the fission yields predicted by SPY. Future experiments producing fission fragments similar to those predicted by the doubly asymmetric fission mode could also reveal the nuclear properties of the corresponding fission fragments. Such future research as well as additional experimental constraints on fission barriers, fission probabilities and fission yields may put the nuclear predictions of fission properties on safer grounds and help us to unravel the still-unsolved mystery concerning the origin of the r-process nuclei in the Universe.

S.G. is F.N.R.S. research associate. S.G. thanks A. Bauswein, H.-T. Janka, S. Hilaire, S. Panebianco, J.-L. Sida and J.-F Lemaître for helpful discussions and sharing their calculations.

References

1. M. Arnould, S. Goriely, K. Takahashi, Phys. Rep. **450**, 97 (2007).
2. S. Wanajo, H.-T. Janka, B. Müller, Astrophys. J. Lett. **726**, L15 (2011).
3. H.-T. Janka, Annu. Rev. Nucl. Part. Sci. **62**, 407 (2012).
4. D. Argast, M. Samland, F.-K. Thielemann, F.Y. Qian, Astron. Astrophys. **416**, 997 (2004).
5. L. Hüdepohl, B. Müller, H.-T. Janka, A. Marek, G.G. Raffelt, Phys. Rev. Lett. **104**, 251101 (2010).
6. T. Fischer, S.C. Whitehouse, A. Mezzacappa, F.-K. Thielemann, M. Liebendörfer, Astron. Astrophys. **517**, A80 (2010).
7. S. Tsuruta, A.G.W. Cameron, Can. J. Phys. **43**, 2056 (1965).
8. J.M. Lattimer, D.N. Schramm, Astrophys. J. **192**, L145 (1974).
9. J.M. Lattimer, F. Mackie, D.G. Ravenhall, D.N. Schramm, Astrophys. J. **213**, 225 (1977).
10. B.S. Meyer, Astrophys. J. **343**, 254 (1989).
11. H.-T. Janka, T. Eberl, M. Ruffert, C.L. Fryer, Astrophys. J. Lett. **527**, L39 (1999).
12. S. Rosswog, M. Liebendörfer, F.-K. Thielemann, M.B. Davies, T. Piran, Astron. Astrophys. **341**, 499 (1999).
13. S. Rosswog, R. Speith, G.A. Wynn, Mon. Not. R. Astron. Soc. **351**, 1121 (2004).
14. R. Oechslin, H.-T. Janka, A. Marek, Astron. Astrophys. **467**, 395 (2007).
15. S. Goriely, A. Bauswein, H.-T. Janka, Astrophys. J. Lett. **738**, L32 (2011).
16. A. Bauswein, S. Goriely, H.-T. Janka, Astrophys. J. **773**, 78 (2013).
17. S. Goriely, J.-L. Sida, J.-F. Lemaître, S. Panebianco, N. Dubray, S. Hilaire, A. Bauswein, H.-T. Janka, Phys. Rev. Lett. **111**, 242502 (2013).
18. O. Just, A. Bauswein, R. Ardevol Pulpillo, S. Goriely, H.-T. Janka, Mon. Not. R. Astron. Soc. **448**, 541 (2015).
19. K. Hotokezaka, K. Kiuchi, K. Kyutoku, H. Okawa, Y.-I. Sekiguchi, M. Shibata, K. Taniguchi, Phys. Rev. D **87**, 024001 (2013).
20. S. Wanajo, Y. Sekiguchi, N. Nishimura, K. Kiuchi, K. Kyutoku, M. Shibata, Astrophys. J. Lett. **789**, L39 (2014).
21. C. Freiburghaus, S. Rosswog, F.-K. Thielemann, Astrophys. J. **525**, L121 (1999).
22. S. Goriely, P. Demetriou, H.-T. Janka, J.M. Pearson, Nucl. Phys. A **758**, 587c (2005).
23. B.D. Metzger, G. Martinez-Pinedo, S. Darbha *et al.*, Mon. Not. R. Astron. Soc. **406**, 2650 (2010).
24. L.F. Roberts, D. Kasen, W.H. Lee, E. Ramirez-Ruiz, Astrophys. J. Lett. **736**, L21 (2011).
25. O. Korobkin, S. Rosswog, A. Arcones, C. Winteler, Mon. Not. R. Astron. Soc. **426**, 1940 (2012).
26. M. Dominik, K. Belczynski, C. Fryer, D.E. Holz, E. Berti, T. Bulik, I. Mandel, R. O'Shaughnessy, Astrophys. J. **759**, 52 (2012).
27. C. Sneden, J.J. Cowan, R. Gallino, Annu. Rev. Astron. Astrophys. **46**, 241 (2008).
28. I.U. Roederer, J.J. Cowan, A.I. Karakas, K.-L. Kratz, M. Lugaro, J. Simmerer, K. Farouqi, C. Sneden, Astrophys. J. **724**, 975 (2010).
29. I.U. Roederer, Astrophys. J. **732**, L17 (2011).

30. L.-X. Li, B. Paczyński, Astrophys. J. **507**, L59 (1998).
31. J. Barnes, D. Kasen, arXiv:1303.5787 (2013).
32. E. Berger, W. Fong, R. Chornock, Astrophys. J. **774**, L23 (2013).
33. N.R. Tanvir, A.J. Levan, A.S. Fruchter, J. Hjorth, R.A. Hounsell, K. Wiersema, R.L. Tunnicliffe, Nature **500**, 547 (2013).
34. F. Matteucci, D. Romano, A. Arcones, O. Korobkin, S. Rosswog, Mon. Not. R. Astron. Soc. **438**, 2177 (2014).
35. Y. Komiya, S. Yamada, T. Suda, M.Y. Fujimoto, Astrophys. J. **783**, 132 (2014).
36. N. Mennekens, D. Vanbeveren, Astron. Astrophys. **564**, A134 (2014).
37. S. Shen, R. Cooke, E. Ramirez-Ruiz, P. Madau, L. Mayer, J. Guedes, arXiv:1407.3796 (2014).
38. F. van de Voort, E. Quataert, P.F. Hopkins, D. Keres, C.-A. Faucher-Giguere, arXiv:1407.7039 (2014).
39. E. Vangioni, S. Goriely, F. Daigne, P. François, submitted to Astron. Astrophys. (2014).
40. A. Bauswein, H.-T. Janka, R. Oechslin, Phys. Rev. D **82**, 084043 (2010).
41. S. Typel, G. Röpke, T. Klähn, D. Blaschke, H.H. Wolter, Phys. Rev. C **81**, 015803 (2010).
42. K. Belczynski, R. O'Shaughnessy, V. Kalogera, F. Rasio, R.E. Taam, T. Bulik, Astrophys. J. Lett. **680**, L129 (2008).
43. P.B. Demorest, T. Pennucci, S.M. Ransom, M.S.E. Roberts, J.W.T. Hessels, Nature **467**, 1081 (2010).
44. J. Antoniadis *et al.*, Science **340**, 448 (2013).
45. Y. Xu, S. Goriely, A. Jorissen, G.L. Chen, M. Arnould, Astron. Astrophys. **549**, A106 (2013) see also `http://www.astro.ulb.ac.be/bruslib`.
46. A.J. Koning, S. Hilaire, M.C. Duijvestijn, AIP Conf. **769**, 1154 (2005).
47. A.J. Koning, D. Rochman, Nucl. Data Sheets **113**, 2841 (2012).
48. S. Goriely, S. Hilaire, A.J. Koning, Astron. Astrophys. **487**, 767 (2008).
49. S. Goriely, N. Chamel, J.M. Pearson, Phys. Rev. C **82**, 035804 (2010).
50. T. Tachibana, M. Yamada, Y. Yoshida, Prog. Theor. Phys. **84**, 641 (1990).
51. H. Koura, T. Tachibana, T. Yoshida, J. Nucl. Sci. Technol., Suppl. **2**, 774 (2002).
52. S. Bjørnholm, J.E. Lynn, Rev. Mod. Phys. **52**, 725 (1980).
53. M.J. Lopéz Jiménez, B. Morillon, P. Romain, Annu. Nucl. Energy **32**, 195 (2005).
54. S. Goriely, M. Samyn, J.M. Pearson, Phys. Rev. C **75**, 064312 (2007).
55. S. Goriely, M. Samyn, J.M. Pearson, M. Onsi, Nucl. Phys. A **750**, 425 (2005).
56. M. Bender, P.-H. Heenen, P. Bonche, Phys. Rev. C **70**, 054304 (2004).
57. S. Perez-Martin, L. M. Robledo, Phys. Rev. C **78**, 014304 (2008).
58. G. Audi, W. Wang, A.H. Wapstra, F.G. Kondev, M. MacCormick, X. Xu, B. Pfeiffer, Chin. Phys. C **36**, 1287 (2012).
59. J.-P. Delaroche, M. Girod, H. Goutte, J. Libert, Nucl. Phys. A **771**, 103 (2006).
60. S.A. Giulani, L.M. Robledo, R. Rodriguez-Guzman, Phys. Rev. C **90**, 054311 (2014).
61. R. Capote *et al.*, Nucl. Data Sheets **110**, 3107 (2009) see also `http://www-nds.iaea.org/RIPL-3`.
62. P. Möller, A.J. Sierk, T. Ichikawa, A. Iwamoto, R. Bengtsson, H. Uhrenholt, S. Aberg, Phys. Rev. C **79**, 064304 (2009).
63. A. Mamdouh, J.M. Pearson, M. Rayet, F. Tondeur, Nucl. Phys. A **679**, 337 (2001).
64. W.D. Myers, W.J. Swiatecki, Phys. Rev. C **60**, 014606 (1999).
65. W.M. Howard, P. Möller, At. Nucl. Data Tables **25**, 219 (1980).
66. J. Erler, K. Langanke, H.P. Loens, G. Martinez-Pinedo, P.-G. Reinhard, Phys. Rev. C **85**, 025802 (2012).
67. J. Sadhukhan, K. Mazurek, A. Baran, J. Dobaczewski, W. Nazarewicz, J.A. Sheikh, Phys. Rev. C **88**, 064314 (2013).
68. S. Goriely, S. Hilaire, A.J. Koning, M. Sin, R. Capote, Phys. Rev. C **79**, 024612 (2009).
69. S. Goriely, S. Hilaire, A.J. Koning, Phys. Rev. C **78**, 064307 (2008).
70. A.V. Ignatyuk, IAEA report, TECDOC-1034 (1998).
71. Y. Kalmykov, C. Özen, K. Lamganke, G. Martinez-Pinedo, P. von Neumann-Cosel, A. Richter, Phys. Rev. Lett. **99**, 202502 (2007).
72. EXFOR database, International Network of Nuclear Reaction Data Centres (NRDC), available at `http://www-nds.iaea.org/exfor/exfor.htm`.
73. S. Goriely, S. Hilaire, A.J. Koning, R. Capote, Phys. Rev. C **83**, 034601 (2011).
74. I.V. Panov, I.Yu. Korneev, T. Rauscher, G. Martinez-Pinedo, A. Kelic-Heil, N.T. Zinner, F.-K. Thielemann, Astron. Astrophys. **513**, A61 (2010).
75. T. Kodoma, K. Takahashi, Nucl. Phys. A. **239**, 489 (1975).
76. I.N. Borzov, S. Goriely, Phys. Rev. C **62**, 035501 (2000).
77. S. Goriely, to be submitted to Nucl. Phys A (2015).
78. A.N. Andreyev, M. Huyse, P. Van Duppen, Rev. Mod. Phys. **85**, 1541 (2013).
79. S. Panebianco, J.-L. Sida, H. Goutte, J.-F. Lemaître, N. Dubray, S. Hilaire, Phys. Rev. C **86**, 064601 (2012).
80. S. Hilaire, M. Girod, Eur. Phys. J. A **33**, 237 (2007).
81. K.-H. Schmidt, B. Jurado, Phys. Rev. Lett. **104**, 212501 (2010).
82. K.-H. Schmidt, B. Jurado, Phys. Rev. C **83**, 061601 (2011).
83. K.-H. Schmidt, B. Jurado, Phys. Proc. **31**, 147 (2012).
84. N. Dubray, D. Regnier, Comput. Phys. Commun. **183**, 2035 (2012).
85. S. Goriely, Astron. Astrophys. **342**, 881 (1999).
86. S. Goriely, A. Bauswein, H.-T. Janka, S. Panebianco, J.-L. Sida, J.-F. Lemaitre, S. Hilaire, N. Dubray, to be published in Nucl. Phys. Astrophys. VI, J. Phys.: Conf. Ser. (2013).
87. B.D. Metzger, A. Bauswein, S. Goriely, D. Kasen, Mon. Not. R. Astron. Soc. **446**, 1115 (2015).
88. I. Petermann, K. Langanke, G. Martínez-Pinedo, I.V. Panov, P.-G. Reinhard, F.-K. Thielemann, Eur. J. Phys. A **48**, 122 (2012).
89. R. Bengtsson, W.M. Howard, Phys. Lett. B **55**, 281 (1975).

90. M.R. Mumpower, G.C. McLaughlin, R. Surman, Astrophys. J. **752**, 117 (2012).
91. I.V. Panov, I.Yu. Korneev, F.-K Thielemann, Astron. Lett. **34**, 189 (2008).
92. Compilation and evaluation of fission yield nuclear data, IAEA-TECDOC-1168 (2000) p. 143.
93. J.J. Cowan, F.-K. Thielemann, J.W. Truran, Phys. Rep. **208**, 267 (1991).
94. R. Hoff, J. Phys. G **24**, S343 (1987).
95. J.J. Mendoza, G. Pinedo, K.-H. Langanke, A. Bauswein, H.-T. Janka, arXiv:1409.6135v1 (2014).
96. S. Goriely, S. Hilaire, M. Girod, S. Péru, Phys. Rev. Lett. **102**, 242501 (2009).
97. P. Möller, J.R. Nix, W.D. Myers, W.J. Swiatecki, SAt. Data Nucl. Data Tables **59**, 185 (1995).
98. J.E. Lynn, *The theory of neutron resonance reactions* (Clarendon press, Oxford, 1968).
99. P. Descouvemont, J. Phys. G **35**, 014006 (2008).
100. Y. Xu, S. Goriely, Phys. Rev. C **86**, 045801 (2012).
101. Y. Xu, S. Goriely, A.J. Koning, S. Hilaire, Phys. Rev. C **90**, 024604 (2014).
102. P. Möller, B. Pfeiffer, K.-L. Kratz, Phys. Rev. C **67**, 055802 (2003).
103. H.V. Klapdor, J. Metzinger, T. Oda, At. Data Nucl. Data Tables **31**, 81 (1984).
104. I.N. Borzov, Phys. At. Nucl. **74**, 1435 (2011).
105. T. Marketin, L. Huther, G. Martínez-Pinedo, in *Nuclei in the Cosmos*, Proceedings of Science (2014) in press.
106. M. Martini, S. Péru, S. Goriely, Phys. Rev. C **89**, 044306 (2014).
107. R. Cayrel *et al.*, Nature **409**, 691 (2001).
108. S. Goriely, M. Arnould, Astron. Astrophys. **379**, 1113 (2001).
109. J.-F. Berger, M. Girod, D. Gogny, Nucl. Phys. A **428**, 23c (1984).
110. J.-F. Berger, M. Girod, D. Gogny, Comput. Phys. Commun. **63**, 365 (1991).
111. H. Goutte *et al.*, Phys. Rev. C **71**, 024316 (2005).
112. N. Dubray, H. Goutte, J.P. Delaroche, Phys. Rev. C **77**, 014310 (2008).
113. R. Bernard, H. Goutte, D. Gogny, W. Younes, Phys. Rev. C **84**, 044308 (2011).